

Observing Topological Phase Transitions with High Harmonic Generation

Alexis Chacón^{1,4*}, Wei Zhu¹, Shane P. Kelly^{1,2}, Alexandre Dauphin³, Emilio Pisanty³, Dasol Kim⁴, Dong Eon Kim⁴, Antonio Picón^{3,5}, Christopher Ticknor¹, Marcelo F. Ciappina^{3,6}, Avadh Saxena¹ and Maciej Lewenstein^{3,7}

¹Center for Nonlinear Studies and Theoretical Division, Los Alamos National Laboratory, Los Alamos, New Mexico 87545, USA

²Physics and Astronomy Department, University of California Riverside, Riverside, California 92521, USA

³ICFO – Institut de Ciències Fotoniques, The Barcelona Institute of Science and Technology, 08860 Castelldefels (Barcelona), Spain

⁴Department of Physics and Center for Attosecond Science and Technology, POSTECH, 7 Pohang 37673, South Korea; Max Planck POSTECH/KOREA Research Initiative, Pohang, 37673, South Korea

⁵Departamento de Química, Universidad Autónoma de Madrid, 28049 Madrid, Spain

⁶Institute of Physics of the ASCR, ELI-Beamlines project, Na Slovance 2, 182 21 Prague, Czech Republic

⁷ICREA, Pg. Lluís Companys 23, 08010 Barcelona, Spain

*achacon@postech.ac.kr

28 January 2020

Topological materials are of interest to both fundamental sciences and advanced technologies, because topological states are robust with respect to perturbations and dissipation. Experimental detection of topological invariants is thus in great demand, but is extremely challenging. Ultrafast laser-matter interactions, and in particular high-harmonic generation (HHG), were proposed several years ago as tools to explore the structural and dynamical properties of various matter targets. Here, we show that the high-harmonic generation signal produced by circularly-polarized lasers contains distinct signatures of the topological phase transition in the paradigmatic Haldane model. In addition to clear shifts of the overall intensity emissivity and harmonic cutoff, the HHG shows an unique circular dichroism which exhibits clear changes in behaviour at the topological phase boundary. Our findings pave the way to understand fundamental questions about the ultrafast electron-hole pair dynamics in topological materials via HHG.

The history of topological order goes back to the discoveries of the Berezinsky-Kosterlitz-Thouless transition in 2D as well as the integer and fractional quantum Hall effects [1–3]. These materials constitute a new paradigm, since they are characterized by a global order parameter: this goes beyond the standard Landau theory of phase transitions, which uses *local* order parameters to describe materials. Topological order, due to its robustness and resistance to perturbations, has already found applications in standards and metrology (most notably, via the integer quantum Hall effect, a key ingredient of the recent revision to the SI system of units [4]), and promises numerous applications from quantum spintronics, valleytronics, to quantum computing. Particularly interesting are possible applications of topological insulators (TI) and superconductors [5]. These systems are insulating in their bulk but have conducting surface states protected by the topological invariant of the bulk. A considerable number of solid-state systems with these properties have been proposed in the recent years, both in the context of real topological materials [6], and synthetic ones, employing ultracold atoms [7], photonic systems [8] and mechanical systems [9], among others. Nevertheless, new methods for the creation and physical characterization of topological phases are still being sought for real

materials. We here focus on the detection of topological phase transitions and different topological phases by the highly non-linear optical responses of the medium, in contrast to recent proposals which employ its linear-optical properties [10, 11].

HHG was first proposed for the detection of molecular structure and orbitals in the seminal work of Itatani *et al.* [12]. In HHG an ultrashort (5–50 fs) intense mid-infrared (MIR) laser pulse causes partial ionization of an electron in an atom/molecule. The resulting electronic wave packet is accelerated in the laser field, returns to the parent ion and recombines there, producing high-order harmonics [13, 14]. The efficiency of this process depends directly on the atomic or molecular orbital that the electron leaves and recombines with, and the electronic and molecular structure of the target can similarly be probed by the re-scattered electron via laser-induced electron diffraction [15, 16].

In the last few years, the subject of HHG from solid-state targets has attracted considerable attention [17–19]. In particular, Vampa and coworkers have studied experimentally the role of intra-band and inter-band currents in ZnO, and use HHG to characterize structural information such as the energy dispersions [20–22] from their nontrivial coupling [23] where inter-band governed the emission. However, depending on material structure Golde *et al.* [23] also showed the intra-band mechanism might govern over inter-band. Additionally, some recent work has also developed real-space approaches that discard the band-structure picture, at least in some regimes [24]. The later shows inter- and intra-band mechanisms can not trivially be disentangled and are of intense discussion for ultrafast sciences. Generally, existing studies have dealt with standard materials, where the topology does not play a role. However, Berry-phase effects have been explored in topologically-trivial materials, through experimental studies of HHG in atomically-thin semiconductors [25] and in quasi-2D models [26], where the sensitivity of harmonic emission to symmetry breaking (specifically, the breaking of inversion symmetry in monolayer MoS₂ and α -quartz) is shown via the appearance of even harmonics.

On more theoretical grounds, the effects of gap closing on the cutoff energy have been discussed by Zurrón *et al.* [27] in graphene, where the first step in the HHG process is initiated by the non-adiabatic crossing of the valence band elec-

tron trajectories through the Dirac points, instead of tunneling. Silva *et al.* [28] showed that HHG can be used to detect a dynamical Mott-insulator transition in strongly-correlated 1D solids, with more recent work by Takayoshi *et al.* [29] probing strongly-correlated spin systems. Bauer and Hansen [30] were the first to show that HHG is sensitive to topological order, by probing the contribution of edge states in a 1D chain analogous to the Su-Schrieffer-Heeger model [31, 32], which they solved using time-dependent density functional theory.

In this work, we push this idea to a natural culmination and show that the circular dichroism of the HHG can be used as a signature of the topological phase transition in 2D materials, such as the paradigmatic Haldane model (HM) [33] – illustrated in Fig. 1. We derive, verify and apply the theory of HHG driven by both linearly and circularly polarized light in a two-band model, fully including the effects of the Berry curvature and its associated connection. We characterize and analyze the HHG spectrum: the intra- and inter-band contributions. Furthermore, our theoretical conclusions are invariant with respect to both the electromagnetic and the Bloch wavefunction gauges (see the Supplementary Material (SM)) and we use separate Bloch-gauge charts of the Brillouin zone (BZ), as required in topological phases [34], where no continuous single-gauge charts exist, to deal with the discontinuity/singularity of dipole and Berry connection for the numerical calculations of HHG (see section 4 in SM). We perform a saddle-point analysis, in which the semi-classical electron-hole pair trajectories include the phases of transition dipole moments to assure the full gauge invariance and the Berry curvatures (in contrast to Ref. [35]).

Our theoretical approach predicts the following: (i) A complete model, which captures the reported features of experiments for both linearly-and circularly-polarized driving lasers [25, 26, 36], and predicts novel behaviours for topologically non-trivial systems; (ii) HHG is extremely sensitive to inversion symmetry (IS) and, in addition, to breaking time-reversal symmetry (TRS); and (iii) the HHG spectrum intensity depends on the topological phases, and the circular dichroism of high harmonic orders is sensitive to crossing a topological phase transition boundary.

1 · The Haldane model

The Haldane model [33], originally introduced as a toy model, represents the first example of an anomalous quantum Hall effect [37], and it captures the essential features of a number of materials [38, 39] – in particular, the quantized transverse (spin) conductivities of the quantum spin Hall effect [40], where the transport happens along protected edge states. Moreover, this model remains solvable and implementable in quantum simulators [41], which makes it a flexible tool for understanding a wide range of phenomena. Specifically, the HM describes a tight-binding Hamiltonian of spinless fermions on a 2D hexagonal lattice with a real nearest-neighbour hopping t_1 , an onsite staggering potential M_0 , and a complex next-to-nearest-neighbour hopping $t_2 e^{i\phi_0}$. The HM belongs to the class of Chern insulators [42], characterized by a topological invariant: an integer, called the Chern number, given by the integral $C := \frac{1}{2\pi} \int_{BZ} \Omega(\mathbf{k}) \cdot d^2\mathbf{k}$ of the Berry curvature $\Omega(\mathbf{k})$ over the Brillouin zone (see the SM for further details). Figure 1(a) depicts the phase diagram in terms of ϕ_0 and M_0 ,

showing three distinct phases: a trivial phase with Chern number $C = 0$ and two different topological phases, with Chern numbers $C = \pm 1$. At the boundary between the phases, the bandgap closes, as shown for the point (Q). In terms of symmetries, the HM has broken inversion symmetry (IS) when the staggering potential M_0 is nonzero, and it breaks time-reversal symmetry (TRS) when the next-nearest-neighbour coupling t_2 has a nonzero complex phase ϕ_0 . In this work, we probe the topological-physics properties of the Haldane model by examining its non-perturbative nonlinear response to a strong laser field. A recent parallel work, complementary to this paper, also examines HHG focusing on the emission of linear driven fields from HM [43].

2 · Inter- and intra-band currents

In a semiconductor or insulator driven by mid-infrared lasers or THz sources, the harmonic emission is governed by the coherent sum of the intra-band $\mathbf{J}_{ra}(t)$ and inter-band $\mathbf{J}_{er}(t)$ current oscillations $\mathbf{J}(t) = \mathbf{J}_{ra}(t) + \mathbf{J}_{er}(t)$ [17, 18]. Those are defined according to,

$$\mathbf{J}_{ra}(t) = e \sum_m \int_{BZ} \mathbf{v}_m(\mathbf{K} + \mathbf{A}(t)) n_m(\mathbf{K}, t) d^3\mathbf{K}, \quad (1)$$

$$\mathbf{J}_{er}(t) = e \frac{d}{dt} \int_{BZ} \mathbf{d}_{cv}^*(\mathbf{K} + \mathbf{A}(t)) \pi(\mathbf{K}, t) d^3\mathbf{K} + \text{c.c.}, \quad (2)$$

where $n_m(\mathbf{K}, t)$ is the m^{th} -band occupation (with the index m running over the valence and conduction bands, i.e. $m = v$ and c , respectively) and $\pi(\mathbf{K}, t)$ is the inter-band coherence; for simplicity, we restrict our study to a two-band model. Here, moreover, $\mathbf{v}_m(\mathbf{k}) = \mathbf{v}_{gr,m}(\mathbf{k}) + \mathbf{v}_{a,m}(\mathbf{k})$ is the m^{th} band classical velocity, $\mathbf{v}_{gr,m}(\mathbf{k}) = \nabla_{\mathbf{k}} \varepsilon_m(\mathbf{k})$ is the particle (i.e. electron or hole) group velocity, and $\mathbf{v}_{a,m}(\mathbf{k}) = -\mathbf{E}(t) \times \boldsymbol{\Omega}_m(\mathbf{k})$ is the anomalous velocity, with $\varepsilon_m(\mathbf{k})$ the bands' energy dispersion and \mathbf{K} the canonical momentum defined in terms of the particle crystal momentum \mathbf{k} and the vector potential $\mathbf{A}(t)$ of the laser's electric field $\mathbf{E}(t) = -\partial_t \mathbf{A}(t)$. (For the derivation of Eqs. (1-2), see the SM.) $\mathbf{d}_{cv}(\mathbf{k})$ is the valence-conduction band dipole transition matrix element. We stress additionally, that the inter-band current contains explicitly information about the Berry curvature through the cross product of the dipole moments (see sections 3.3, 3.5 and 3.6 of the SM). This is an important finding, since in 2D materials the integral of the Berry curvature over the BZ is the topological invariant, i.e. the Chern Number. In Fig. 1(Y) we depict a cartoon of the HHG physical process which takes place in topological materials, mainly for linear driven laser.

Via our semiclassical saddle-point analysis we find the following: (1) The electron-hole pair is likely excited around the K' point and less probably around the Γ or K , points since the energy gap is larger at those points compared to K' , for this Haldane model. (2) The electron-hole pair is propagated by the driving laser field along the path indicated with black dashed line of the BZ emitting intra-band harmonics in the process. This propagation follows the laser vector potential in the momentum plane, with the real-space motion (and thus the intra-band current) governed by the group velocity produced by the energy-band dispersion as well as an anomalous velocity caused by the Berry curvature. (3) Finally, the electron can recombine with its hole and release its energy as a photon. This inter-band emission carries traces of the material's

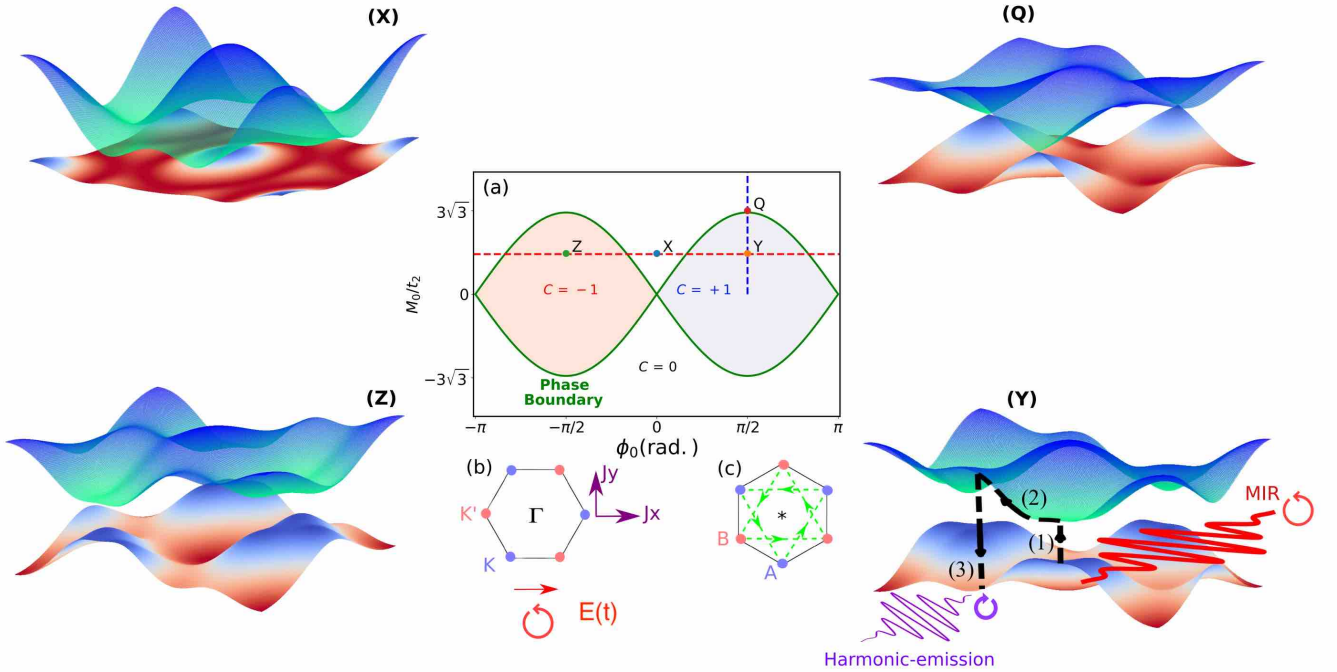


Figure 1 | Phase diagram and band structures of the Haldane model. (a) Phase diagram in the plane $(\phi_0, M_0/t_2)$, with the different phases labelled by their Chern number C ; the green line shows the boundary of the topological phase transition. The band-structure diagrams correspond to the points X, Y, Z and Q as marked in (a), with the point Q at the phase transition showing the gapless Dirac cone at the K point. (Y) and (Z) depict the band structure when the conduction-band topological invariants are $C = \pm 1$ at the phase points $\phi_0 = \pm\pi/2$ and $M_0 = 2.54t_2$. (Y) shows how the mid-infrared, MIR or laser-source oscillations (red-solid line) drive the topological material; this can be with both linear and circular polarizations. We also depict a physical cartoon of the electron-hole pair dynamics driven by a linear polarized laser, i.e. creation, propagation and annihilation or recombination by the black-dashed lines with arrows, and finally the subsequent harmonic emission (violet oscillations). The dashed lines in (a) indicate the cuts used for the parameter scans below. Panels (b) and (c) show the Brillouin zone and the real-space lattice of the Haldane model with the couplings in use.

topological features via both Berry-curvature contributions to the action accrued in the continuum traversal as well as in the dipole matrix elements that mediate the transition, for more details see SM.

We start by analyzing the recent HHG experiment of Luu and Wörner [26] on α -quartz (SiO_2). Since a cut along the z -direction of this crystal has an approximate honeycomb lattice structure, we use the trivial limit of the HM to validate our theory (see SM). Due to the breaking of IS in α -quartz, the HHG spectrum contains even harmonic orders (HOs), shown in Fig. 2(a), mainly along the perpendicular emission configuration. Our theory shows that the inter-band contribution has a larger magnitude than the intra-band current (see SM). Generally, the experimental features of Ref. 26 are qualitatively reproduced by our theory (see Fig. 2(b)). Moreover, this approach qualitatively agrees with Liu *et al.*'s experiment reported for MoS_2 [25] and manage to reproduce linear cutoff law too [21]. Finally, as further validation, we present in the SM a scaling analysis of the harmonic cutoff with respect to the driving-field amplitude, which exhibits a linear scaling in good agreement with previous literature [17, 21].

3 · Signatures of topological phases in HHG

We now address the question of whether HHG is an observable sensitive to (i) different topological phases

and (ii) topological transitions. To this end, in Fig. 2 we show the full calculated HHG radiation spectrum, $I_{\text{HHG}}(\omega) = \omega^2 (|J_x(\omega)|^2 + |J_y(\omega)|^2)$ produced by linearly-polarized (Fig. 2(c)) and circularly-polarized (Fig. 2(d)) driving lasers, comparing instances from the trivial and the topologically-nontrivial phase at equal bandgaps. For a linearly-polarized driving laser, the harmonic emission exhibits relatively small differences between the two phases at the level of the total spectrum (though the vector character of this emission does show stronger differences [43]). In our results, we observe an enhancement of about one order of magnitude for even-order harmonics in the low spectral region, i.e. the 2nd, 4th and 6th harmonics.

For a circularly-polarized driver, on the other hand, shown in Fig. 2(d), the spectra produced by the different topological phases exhibit far greater differences, including in particular: (1) a considerable enhancement about four orders of magnitude in plateau harmonics on the topological phase as compared with the trivial phase, (2) a shorter cut-off for the topological emissions in comparison to the trivial, and (3) an asymmetry yield between the co-rotating $(3n+1)$ and contra-rotating $(3n+2)$ harmonic orders in plateau harmonics. As such, it is clear that circularly-polarized drivers have significant potential in bringing out the signatures of the topological phase in the harmonic spectrum, and we will focus on them

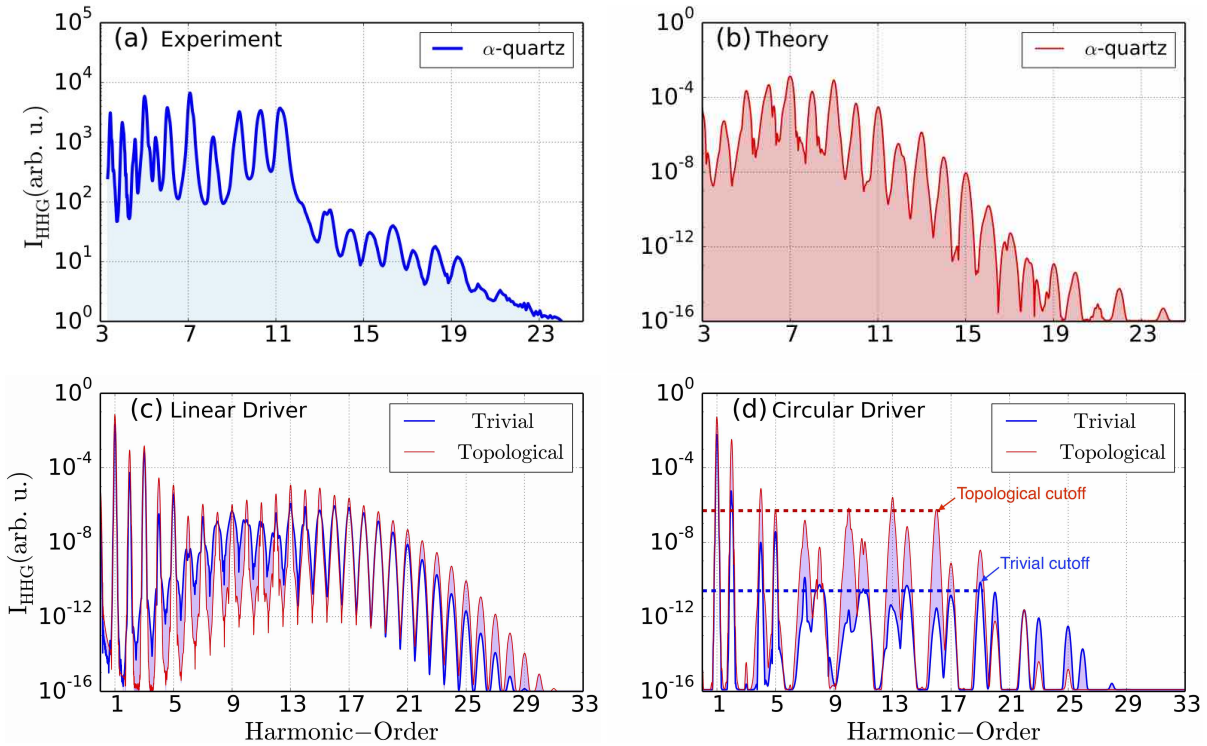


Figure 2 | High-order harmonics for trivial and nontrivial topological materials. (a) Experimental and (b) theoretical comparison of the HHG spectrum from an α -quartz crystal. Both the theoretical and experimental data are averaged along the parallel and perpendicular harmonic emission with respect to a linearly-polarized MIR 800 nm laser. In our simulations we employ a laser field that mimics the one used by Luu & Wörner [26]. Calculations of HHG spectrum for linear polarized driven-laser along the Γ - K crystal orientation (cf. Fig. 1(b)). In (c,d) we show the harmonic emission from equal-bandgap instances from the trivial and topological phases driven by lasers with (c) linear polarization along Γ - K and (d) right-circular polarization; the violet areas indicate the difference in the emission between the two phases. In (c,d) we use $t_1 = 2.04$ eV, $t_2 = t_1/3$ and $M_0 = 2.54 t_2$, with lattice constant $a_0 = 1$ Å, driven by a laser centered at $3.25\text{ }\mu\text{m}$ ($\omega_0 = 0.014$ a.u.) with a Gaussian envelope with 14-cycles FWHM and a peak electric-field strength of $E_0 = 0.0045$ a.u. ($I_0 = 7.0 \times 10^{11}$ W/cm 2), and we use a dephasing time of $T_2 = 5.2$ fs. The magnetic flux of the trivial and non-trivial phases, $\phi_0 = 0.06$ and $\phi_0 = 1.16$ rad, resp., are chosen to give equal bandgaps of $E_g = 3.0$ eV.

for the rest of this work.

The circularly-driven spectra of Fig. 2(d) are also noticeably different from the HHG driven by linearly-polarized pulses, in that they exhibit a clear selection rule, with harmonics of order $3n$ ($3n \pm 1$) forbidden (allowed) for integer n . This selection rule is identical to that observed in the well-known ‘bircircular’ field configuration – two counter-rotating circularly-polarized drivers at frequencies ω_0 and $2\omega_0$ [44] – and it stems from the same origin, a dynamical symmetry of the system, which combines a rotation by 120° with a time delay [45], and which has also been applied to molecules [46–48] as well as solids [36, 49–52] and even plasmonic metamaterials [53]. In our case, however, the generating medium – the Haldane Model on a hexagonal lattice – is symmetric under 120° rotations, but it lacks reflection symmetry, which allows it to respond nontrivially to the different helicities of circularly-polarized driving lasers, much like p states in noble-gas atoms [54, 55] and chiral molecules [56, 57], which points to the circular dichroism of the optical response (i.e. the difference in response to left- and right-handed circularly-polarized drivers) as a natural place to look for signatures of the topological phase of the material.

4 · Dichroism of the topological harmonic spectra

As an initial test of this idea, we show in Figs. 3(a) and 3(b) the total harmonic spectra produced in topologically trivial

and nontrivial phases, respectively, when driven by a right- and left-circularly polarized (RCP and LCP, shown in blue and red, resp.) laser pulse. Here the topologically-nontrivial phase shows a distinct increase in harmonic order responses of the form $k = 3n + 1$, which co-rotate with the driving laser due to the usual selection rules, when driven by an RCP laser as compared with an LCP driver, while the topologically-trivial phase shows a small *decrease* in the emission of those harmonics. (In absolute terms, this combination of laser helicities matches that of the next-nearest-neighbour coupling $t_2 e^{i\phi_0}$, as shown in Fig. 1(c); if a negative ϕ_0 is chosen instead, the effect reverses direction.)

This observation indicates that, indeed, the circular dichroism (CD) of the harmonic emission carries clear information about the topological phase performing the emission (the CD is invariant under the electromagnetic minimum-coupling gauge, as discussed in section 7.1 of SM), and we focus on it for the rest of this work. We define, in particular,

$$\text{CD}_k = \frac{I_{k,\text{RCP}}^{(+)} - I_{k,\text{LCP}}^{(-)}}{I_{k,\text{RCP}}^{(+)} + I_{k,\text{LCP}}^{(-)}}, \quad (3)$$

that is, the normalized difference in harmonic response driven by left- and right-handed circularly-polarized drivers, for harmonic orders $k = 3n + 1$. (For the counter-rotating harmonics $k = 3n + 2$, the signs in the superscripts should be re-

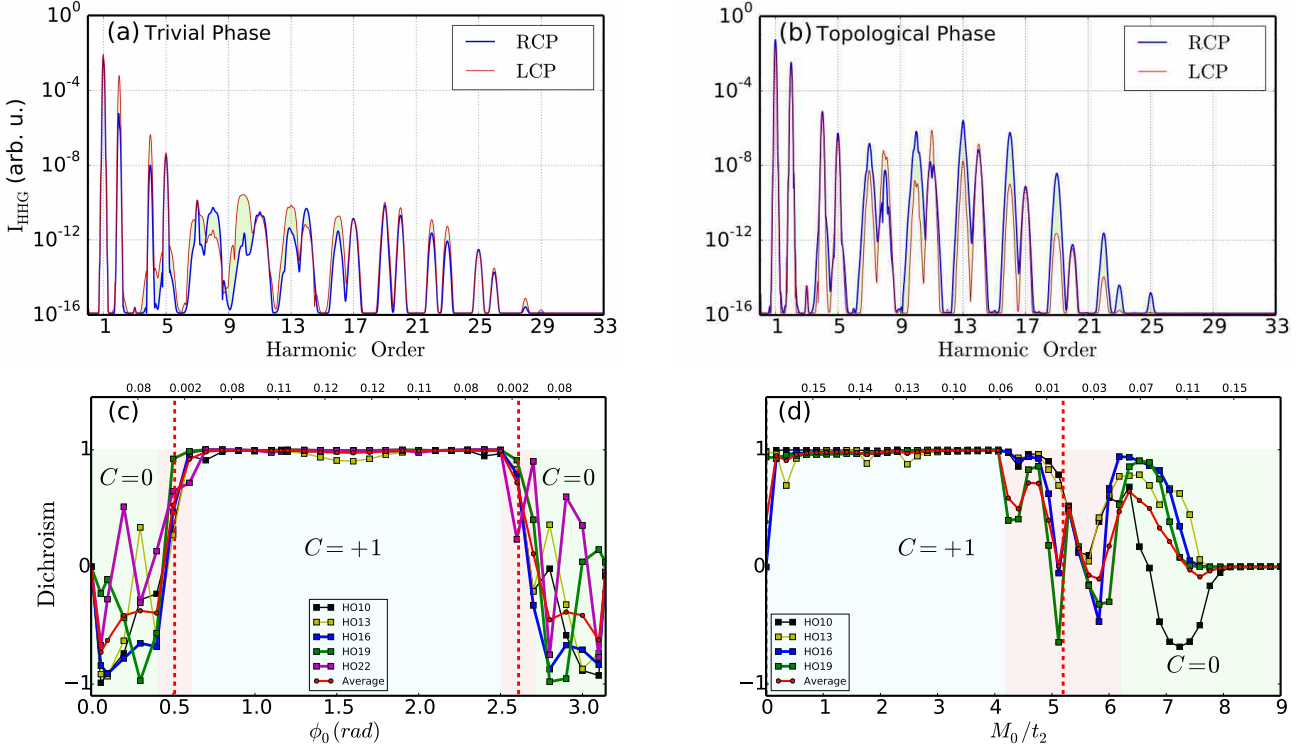


Figure 3 | Topological phase transition in the circular dichroism of HHG. (a,b) Harmonic spectra of equal-bandgap instances from the trivial and the topological phase, respectively, driven by right-circular and left-circularly polarized lasers, with the difference between those two emissions shadowed in green –laser and material parameters are the same as in Fig. (2d). (c,d) Circular dichroism (CD), as defined in Eq. (3), for the magnetic-flux and staggering potential parameter scans marked with dashed lines in Fig. 1, for the plateau harmonics. Top horizontal axes show the energy bandgap E_g in atomic units as a function of ϕ_0 (c) and M_0/t_2 (d), respectively. The trivial and topological regions are shaded green and blue, with the critical region shaded red. The dichroism shows clear changes in behaviour at the topological phase transition. The simulation parameters are the same as in Fig. 4.

versed.) Here the circular dichroism is defined in terms of the circular components of the harmonic emission, $I_{k,\nu}^{(\pm)} = (k\omega_0)^2 |J_{x,\nu}(k\omega_0) \pm i J_{y,\nu}(k\omega_0)|^2$, with $J_{x,\nu}$ and $J_{y,\nu}$ the x and y components of the spectral current driven by a $\nu = \text{RCP}, \text{LCP}$ laser.

Our main result is shown in Figs. 3(c,d), which plot the circular dichroism for the co-rotating plateau harmonics over the two different phase-space cuts of Fig. 1(a) – one scanning over ϕ_0 with M_0 constant, and the other at $\phi_0 = \pi/2$ and scanning over M_0/t_2 . In both cuts we observe a clear plateau in the circular dichroism in the topological phase with Chern number $C = +1$, at $\text{CD} \approx 1$, which only deviates from this behaviour as the topological phase boundary is approached. In the trivial phase, on the other hand, the circular dichroism exhibits a more irregular behaviour, with largely negative values on the ϕ_0 scan, which clearly differentiate it from the topological phase. On the other hand, in the M_0/t_2 scan, once the topological phase boundary is crossed, the circular dichroism disappears relatively quickly as M_0/t_2 increases. This effect can be understood rather simply, since in the $M_0 \gg t_2$ limit, the material's Hamiltonian is dominated by the staggering potential M_0 , which is reflection-symmetric, and does not support a circularly-dichroic response. However, the most notable aspect of the CD spectra is that, even for instances of the Haldane model which – at the level of the Hamiltonian – are ‘equally chiral’, in the sense of having identical M_0/t_2 ratios, the circular dichroism still exhibits clear variations depending on the

topological phase the system is in. In other words, then, the high-harmonic circular dichroism response forms a clear signature of the topological phase of the system.

There is also a clear transition regime between the two topological phases, shown shaded pink in Figs. 3(c,d), where the circular dichroism (particularly in the M_0/t_2 scan) takes on irregular values. At the topological phase boundary, the bandgap closes, as it must do whenever the Chern number changes value, at these points the material becomes a semimetal with exact graphene-like Dirac cones; in the critical region around them (see panel (Q) in Fig. 1), the material is a semiconductor with a negligible gap which is similarly permissive to nonadiabatic transitions. Within this critical region, as in graphene [51], the lowered bandgap produces a much higher electron-hole population, which naturally raises the harmonic emission, as we show in Fig. 4, which displays the total emission for both of the phase-space scans of Fig. 3 for each of the driving helicities. This raised emission acts naturally as a marker that the topological phase boundary itself has been reached, to complement the circular dichroism as a signature of which topological phase the material is in. Moreover, the total-emission scans of Fig. 4 confirm that the features observed previously also hold more broadly over the phase diagram: for one, the topologically-nontrivial phase shows a higher emissivity than the trivial material, at similar bandgaps (shown in Fig. 4(c,f)), and, similarly, there are noticeable changes in the harmonic cutoff as well.

These features in the harmonic intensity and the circular

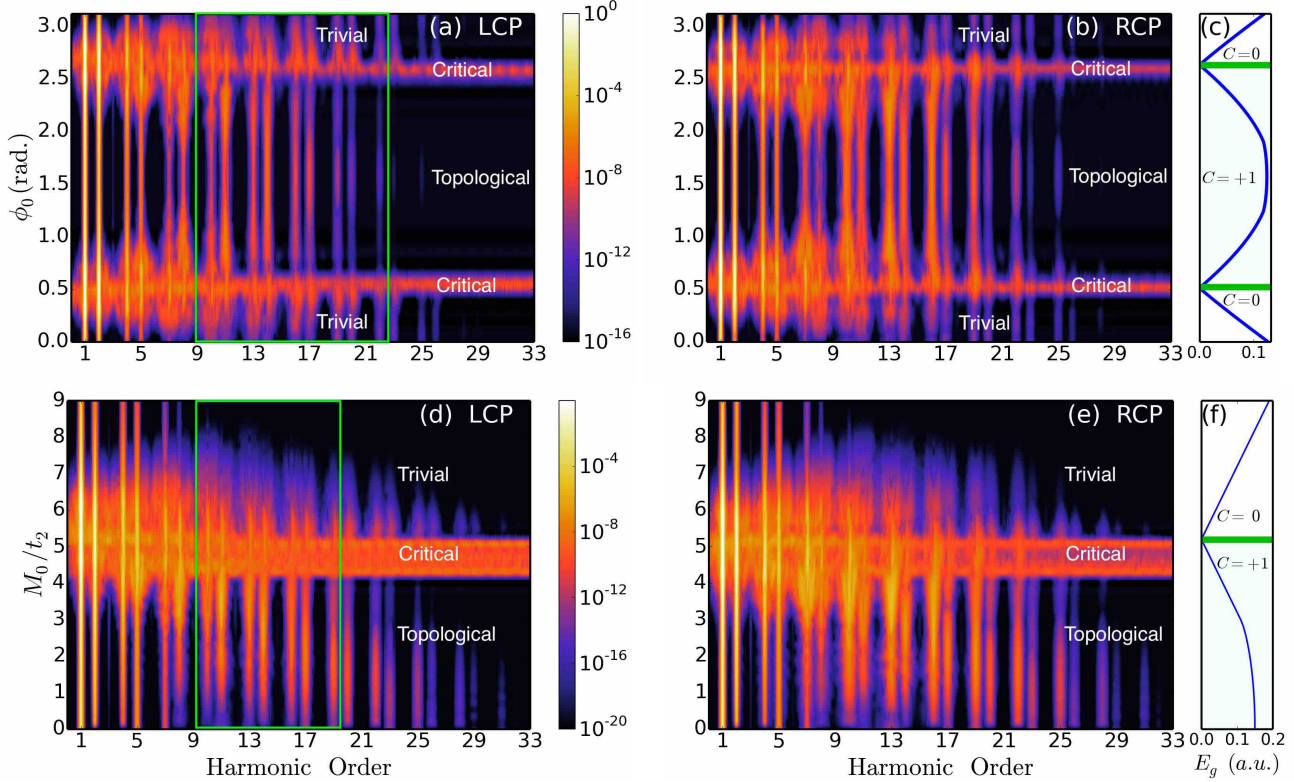


Figure 4 | Variation of the harmonic spectrum for circularly-polarized drivers. (a,b) Harmonic spectrum for the magnetic-flux parameter scan indicated with the red dashed line in Fig. (1a), driven by LCP and RCP light, respectively, with ϕ_0 ranging over a 60-point scan of the interval $[0, \pi]$ and the staggering potential held fixed at $M_0 = 2.54t_2$. At the critical region, where the bandgap closes between the two phases (as indicated in (c), which charts the bandgap), the harmonic emission increases, as carrier creation is much easier. The signature of the topological phase is in the circular dichroism (the difference between the RCP-driven signal in (b) and the LCP-driven signal in (a), which we plot in Fig. 3 for the harmonics in the green box). (d,e,f) Identical plots, for the staggering-potential scan marked by the blue dashed line in Fig. (1a), varying M_0/t_2 at fixed magnetic flux of $\phi_0 = \frac{\pi}{2}$.

dichroism, we should point out, depend (sometimes sensitively) on the dephasing time T_2 in our calculation, which we describe in more detail in the SM. Since the electron-hole trajectory mechanism is modified by the dephasing time, particularly for long trajectories, the harmonic intensity, and from it the circular dichroism, inherit this effect, as expected [18, 21, 58]. On the other hand, and somewhat surprisingly, in the topological phase the circular dichroism is more robust against dephasing than in the trivial phase, particularly for the $k = 3n + 1$ co-rotating harmonics, which again points to a clear role of the material's topology in its harmonic response, and cements the interaction between the two as a clear target for future investigation. In summary, our theory suggests that the HHG spectrum is able to: (1) probe topological-phase transitions, (2) test topological invariants by using the circular dichroism of the co-rotating harmonics, and (3) be extremely sensitive to symmetry breaking of time-reversal and inversion. Those are important results, since (i) our theory can be applied to a larger range of topological materials with similar band-gap properties described in this manuscript and extended to THz sources [59]. Another possible application could be Bi_2Se_3 , which is a good candidate for topological insulator; possible layer-thick modifications could be created in this material in order to control the topological transition as in Ref. [60]; (ii) THz sources also open a path to access HHG in topological materials by pushing the driving photon energy well below the band-gap in two different topological

orders; (iii) this opens also new questions about exploring the dynamics in strongly-correlated systems with spin-orbit couplings and degeneracies.

5 • Methods

The derivation of the inter-band, intra-band currents and semi-conductor Bloch equations that describe the laser-crystal interactions in a topological solid material is presented in the SM. There we also discuss the details of the derivation of gauge-invariant saddle point equations describing quasi-classical electron-hole trajectories, as well as the relationship between the Berry curvature and dipole matrix elements for both the inter- and intra-band contributions to the spectrum. We additionally show in the SM the fundaments of the HM, and we provide additional evidence of the influence of the topological phase transition on the HHG emission.

Acknowledgements

We thank T. T. Luu and H. J. Wörner for providing experimental data in editable format. A. C. thanks D. Baykusheva for running extra calculations of Figs. 3 and 4, in the supercomputer Sherlock at SLAC, and for useful discussions of the CD results, also to N. Aguirre and A. Adedoyin for suggestions in technical details of numerical implementations. We acknowledge the Spanish Ministry MINECO (National Plan 15 Grant: FISICATEAMO No. FIS2016-79508-P, SEVERO OCHOA No. SEV-2015-0522, FPI), European Social Fund, Fundació

Cellex, Generalitat de Catalunya (AGAUR Grant No. 2017 SGR 1341 and CERCA/Program), ERC AdG OSYRIS, EU FETPRO QUIC, and the National Science Centre, Poland-Symfonia Grant No. 2016/20/W/ST4/00314. E. P. acknowledges CELLEX-ICFO-MPQ Fellowship funding. A. P. acknowledges funding from Comunidad de Madrid through TALENTO grant ref. 2017-T1/IND-5432. M. F. C. thanks support of the project Advanced research using high intensity laser produced photons and particles (CZ.02.1.01/0.0/0.0/16 019/0000789) from European Regional Development Fund (ADONIS). S. P. K. acknowledges financial support from the UC Office of the President through the UC Laboratory Fees Research Program, Award Number LGF-17- 476883.

A. C., W. Z., S. K., C. T. and A. S. acknowledge support from LDRD No. 2160587 and the Science Campaigns, Advanced Simulation, and Computing and LANL, which is operated by LANS, LLC for the NNSA of the U.S. DOE under Contract No. DE-AC52-06NA25396 CNLS-LANL. A. C., D. K. and D. E. K. acknowledge support from Max Planck POSTECH/KOREA Research Initiative Program [Grant No 2016K1A4A4A01922028] through the National Research Foundation of Korea (NRF) funded by Ministry of Science, ICT & Future Planning, partly by Korea Institute for Advancement of Technology (KIAT) grant funded by the Korea Government (MOTIE) (P0008763, The Competency Development Program for Industry Specialist).

References

- [1] J. M. Kosterlitz. Nobel lecture: Topological defects and phase transitions. *Rev. Mod. Phys.* **89** no. 4, p. 040 501 (2017). Nobel Prize lecture.
- [2] K. von Klitzing. The quantized Hall effect. *Rev. Mod. Phys.* **58** no. 3, pp. 519–531 (1986). Nobel Prize lecture.
- [3] H. L. Stormer. Nobel lecture: The fractional quantum Hall effect. *Rev. Mod. Phys.* **71** no. 4, pp. 875–889 (1999). Nobel Prize lecture.
- [4] D. Haddad et al. Invited article: A precise instrument to determine the Planck constant, and the future kilogram. *Rev. Sci. Instrum.* **87** no. 6, p. 061 301 (2016).
- [5] X.-L. Qi and S.-C. Zhang. Topological insulators and superconductors. *Rev. Mod. Phys.* **83** no. 4, pp. 1057 –1110 (2011). arXiv:1008.2026.
- [6] M. Z. Hasan and C. L. Kane. Colloquium: Topological insulators. *Rev. Mod. Phys.* **82** no. 4, pp. 3045–3067 (2010). arXiv:1002.3895.
- [7] N. Goldman, G. Juzeliunas, P. Öhberg and I. B. Spielman. Light-induced gauge fields for ultracold atoms. *Rep. Prog. Phys.* **77** no. 12, p. 126 401 (2014). arXiv:1308.6533.
- [8] T. Ozawa et al. Topological photonics. *Rev. Mod. Phys.* **91** no. 1, p. 015 006 (2019). arXiv:1802.04173.
- [9] S. D. Huber. Topological mechanics. *Nat. Phys.* **12** no. 7, p. 621 (2016).
- [10] W. J. M. Kort-Kamp. Topological phase transitions in the photonic spin Hall effect. *Phys. Rev. Lett.* **119**, p. 147 401 (2017). arXiv:1707.02057.
- [11] D. T. Tran, A. Dauphin, A. G. Grushin, P. Zoller and N. Goldman. Probing topology by “heating”: Quantized circular dichroism in ultracold atoms. *Sci. Adv.* **3** no. 8, p. e1701 207 (2017). arXiv:1704.01990.
- [12] J. Itatani et al. Tomographic imaging of molecular orbitals. *Nature* **432** no. 432, pp. 867–871 (2004).
- [13] P. B. Corkum. Plasma perspective on strong field multi-photon ionization. *Phys. Rev. Lett.* **71**, p. 1994 (1993).
- [14] M. Lewenstein, P. Balcou, M. Y. Ivanov, A. L’Huillier and P. B. Corkum. Theory of high-harmonic generation by low-frequency laser fields. *Phys. Rev. A* **49**, p. 2117 (1994).
- [15] T. Zuo, A. D. Bandrauk and P. B. Corkum. Laser-induced electron diffraction: a new tool for probing ultrafast molecular dynamics. *Chem. Phys. Lett.* **259**, p. 313 (1996). HAL eprint.
- [16] B. Wolter et al. Ultrafast electron diffraction imaging of bond breaking in di-ionized acetylene. *Science* **354**, pp. 308–312 (2016). UPCommons eprint.
- [17] S. Ghimire et al. Observation of high-order harmonic generation in a bulk crystal. *Nat. Phys.* **7** no. 2, pp. 138–141 (2011). OSU eprint.
- [18] G. Vampa and T. Brabec. Merge of high harmonic generation from gases and solids and its implications for attosecond science. *J. Phys. B: At. Mol. Opt. Phys.* **50** no. 8, p. 083 001 (2017).
- [19] E. N. Osika et al. Wannier-bloch approach to localization in high-harmonics generation in solids. *Phys. Rev. X* **7** no. 2, p. 021 017 (2017).
- [20] G. Vampa et al. Linking high harmonics from gases and solids. *Nature* **522** no. 7557, p. 462 (2015). JASL eprint.
- [21] G. Vampa, C. R. McDonald, G. Orlando, P. B. Corkum and T. Brabec. Semiclassical analysis of high harmonic generation in bulk crystals. *Phys. Rev. B* **91** no. 6, p. 064 302 (2015). JASL eprint.
- [22] G. Vampa et al. All-optical reconstruction of crystal band structure. *Phys. Rev. Lett.* **115** no. 19, p. 193 603 (2015). JASL eprint.
- [23] D. Golde, T. Meier and S. W. Koch. High harmonics generated in semiconductor nanostructures by the coupled dynamics of optical inter- and intraband excitations. *Phys. Rev. B* **77** no. 7, p. 075 330 (2008).
- [24] H. Lakhotia, M. Zhan, H.-Y. Kim and E. Goulielmakis. Real space approach to high harmonic generation in solids (Conference Presentation). In M. Schultze, E. Goulielmakis and T. Brabec (eds.), *Advances in Ultrafast Condensed Phase Physics*, vol. 10673. International Society for Optics and Photonics (SPIE, 2018), p. 106730M.
- [25] H. Liu et al. High-harmonic generation from an atomically thin semiconductor. *Nat. Phys.* **13** no. 3, p. 262 (2017). Stanford eprint.
- [26] T. T. Luu and H. J. Wörner. Measurement of the Berry curvature of solids using high-harmonic spectroscopy. *Nat. Commun.* **9** no. 1, p. 916 (2018).
- [27] O. Zurrón, A. Picón and L. Plaja. Theory of high-order harmonic generation for gapless graphene. *New J. Phys.* **20** no. 20, p. 053 033 (2018).
- [28] R. E. F. Silva, I. V. Blinov, A. N. Rubtsov, O. Smirnova and M. Ivanov. High-harmonic spectroscopy of ultrafast many- body dynamics in strongly correlated systems. *Nat. Photon.* **12** no. 2, pp. 266–270 (2018). arXiv:1704.08471.

- [29] S. Takayoshi, Y. Murakami and P. Werner. High-harmonic generation in quantum spin systems. *Phys. Rev. B* **99** no. 18, p. 184303 (2019). arXiv:1901.07588.
- [30] D. Bauer and K. K. Hansen. High-harmonic generation in solids with and without topological edge states. *Phys. Rev. Lett.* **120** no. 6, p. 177401 (2018). arXiv:1711.05783.
- [31] H. Drüeke and D. Bauer. Robustness of topologically sensitive harmonic generation in laser-driven linear chains. *Phys. Rev. A* **99** no. 5, p. 053402 (2019). arXiv:1901.01437.
- [32] W. Su, J. Schrieffer and A. J. Heeger. Solitons in polyacetylene. *Phys. Rev. Lett.* **42**, p. 1698 (1979).
- [33] F. D. M. Haldane. Model for a quantum Hall effect without Landau levels: Condensed-matter realization of the “parity anomaly”. *Phys. Rev. Lett.* **61** no. 18, pp. 2015–2018 (1988).
- [34] M. Kohmoto. Topological invariant and the quantization of the Hall conductance. *Ann. Phys.* **160** no. 2, pp. 343–354 (1985).
- [35] F. Yang and R.-B. Liu. Berry phases of quantum trajectories of optically excited electron-hole pairs in semiconductors under strong terahertz fields. *New J. Phys.* **15** no. 11, p. 115005 (2013). arXiv:1211.3021.
- [36] N. Saito et al. Observation of selection rules for circularly polarized fields in high-harmonic generation from a crystalline solid. *Optica* **4** no. 11, pp. 1333–1336 (2017).
- [37] N. R. Cooper, J. Dalibard and I. B. Spielman. Topological bands for ultracold atoms. *Rev. Mod. Phys.* **91** no. 1, p. 015005 (2019). arXiv:1803.00249.
- [38] B. A. Bernevig, T. L. Hughes and S.-C. Zhang. Quantum spin Hall effect and topological phase transition in HgTe quantum wells. *Science* **314** no. 5806, pp. 1757–1761 (2006). arXiv:cond-mat/0611399.
- [39] M. König et al. Quantum spin Hall insulator state in HgTe quantum wells. *Science* **318** no. 5851, pp. 766–770 (2007). arXiv:0710.0582.
- [40] C. L. Kane and E. J. Mele. Quantum spin Hall effect in graphene. *Phys. Rev. Lett.* **95** no. 22, p. 226801 (2005). arXiv:cond-mat/0411737.
- [41] G. Jotzu et al. Experimental realization of the topological Haldane model with ultracold fermions. *Nature* **515** no. 7526, p. 237 (2014). arXiv:1406.7874.
- [42] C.-K. Chiu, J. C. Y. Teo, A. P. Schnyder and S. Ryu. Classification of topological quantum matter with symmetries. *Rev. Mod. Phys.* **88** no. 3, p. 035005 (2016). arXiv:1505.03535.
- [43] R. Silva, A. Jiménez-Galán, B. Amorim, O. Smirnova and M. Ivanov. Topological strong-field physics on sub-laser-cycle timescale. *Nat. Photon.* **13** no. 12, pp. 849–854 (2019). arXiv:1806.11232.
- [44] A. Fleischer, O. Kfir, T. Diskin, P. Sidorenko and O. Cohen. Spin angular momentum and tunable polarization in high-harmonic generation. *Nat. Photon.* **8** no. 7, pp. 543–549 (2014). arXiv:1310.1206.
- [45] O. E. Alon, V. Averbukh and N. Moiseyev. Selection rules for the high harmonic generation spectra. *Phys. Rev. Lett.* **80** no. 17, pp. 3743–3746 (1998).
- [46] F. Mauger, A. D. Bandrauk and T. Uzer. Circularly polarized molecular high harmonic generation using a bicircular laser. *J. Phys. B: At. Mol. Opt. Phys.* **49** no. 10, p. 10LT01 (2016). HAL eprint.
- [47] D. Baykusheva, M. S. Ahsan, N. Lin and H. J. Wörner. Bicircular high-harmonic spectroscopy reveals dynamical symmetries of atoms and molecules. *Phys. Rev. Lett.* **116** no. 12, p. 123001 (2016). ETH eprint.
- [48] K.-J. Yuan and A. D. Bandrauk. Symmetry in circularly polarized molecular high-order harmonic generation with intense bicircular laser pulses. *Phys. Rev. A* **97** no. 2, p. 023408 (2018).
- [49] S. A. Sørngård, S. I. Simonsen and J. P. Hansen. High-order harmonic generation from graphene: Strong attosecond pulses with arbitrary polarization. *Phys. Rev. A* **87** no. 5, p. 053803 (2013).
- [50] Z.-Y. Chen and R. Qin. Circularly polarized extreme ultraviolet high harmonic generation in graphene. *Opt. Express* **27** no. 3, pp. 3761–3770 (2019).
- [51] Óscar Zurrón-Cifuentes, R. Boyero-García, C. Hernández-García, A. Picón and L. Plaja. Optical anisotropy of non-perturbative high-order harmonic generation in gapless graphene. *Opt. Express* **27** no. 5, pp. 7776–7786 (2019).
- [52] A. Jiménez-Galán, R. Silva, O. Smirnova and M. Ivanov. Ultrafast topology for strong-field valleytronics (2019). arXiv:1910.07398.
- [53] K. Konishi et al. Polarization-controlled circular second-harmonic generation from metal hole arrays with three-fold rotational symmetry. *Phys. Rev. Lett.* **112** no. 13, p. 135502 (2014).
- [54] L. Medišauskas, J. Wragg, H. van der Hart and M. Y. Ivanov. Generating isolated elliptically polarized attosecond pulses using bichromatic counterrotating circularly polarized laser fields. *Phys. Rev. Lett.* **115** no. 15, p. 153001 (2015). arXiv:1504.06578.
- [55] E. Pisanty and A. Jiménez-Galán. Strong-field approximation in a rotating frame: High-order harmonic emission from p states in bicircular fields. *Phys. Rev. A* **96** no. 6, p. 063401 (2017). arXiv:1709.00397.
- [56] Y. Harada, E. Haraguchi, K. Kaneshima and T. Sekikawa. Circular dichroism in high-order harmonic generation from chiral molecules. *Phys. Rev. A* **98** no. 2, p. 021401 (2018). HUSCAP eprint.
- [57] D. Ayuso, P. Decleva, S. Patchkovskii and O. Smirnova. Chiral dichroism in bi-elliptical high-order harmonic generation. *J. Phys. B: At. Mol. Opt. Phys.* **51** no. 6, p. 06LT01 (2018).
- [58] G. Vampa et al. Theoretical analysis of high-harmonic generation in solids. *Phys. Rev. Lett.* **113** no. 7, p. 073901 (2014). JASL eprint.
- [59] P. Rodriguez-Lopez, W. J. M. Kort-Kamp, D. A. R. Dalvit and L. M. Woods. Nonlocal optical response in topological phase transitions in the graphene family. *Phys. Rev. Materials* **2**, p. 014003 (2018). arXiv:1711.06311.
- [60] M. Neupane et al. Observation of quantum-tunnelling-modulated spin texture in ultrathin topological insulator Bi₂Se₃ films. *Nat. Commun.* **5** no. 3841, pp. 1–7 (2014). arXiv:1404.2830.

- [61] E. Blount. Formalisms of band theory. In F. Seitz and D. Turnbull (eds.), *Solid State Physics*, vol. 13, pp. 305–373 (Academic Press, 1962).
- [62] S. Y. Kruchinin, M. Korbman and V. S. Yakovlev. Theory of strong-field injection and control of photocurrent in dielectrics and wide band gap semiconductors. *Phys. Rev. B* **87** no. 11, p. 115201 (2013).
- [63] M. Spivak. *A comprehensive introduction to differential geometry* (Publish or Perish, Houston, 1999).
- [64] P. G. Hawkins, M. Y. Ivanov and V. S. Yakovlev. Effect of multiple conduction bands on high-harmonic emission from dielectrics. *Phys. Rev. A* **91** no. 1, p. 013405 (2015). arXiv:1409.5707.
- [65] I. Floss et al. *Ab initio* multiscale simulation of high-order harmonic generation in solids. *Phys. Rev. A* **97** no. 1, p. 011401 (2018). arXiv:1705.10707.
- [66] V. S. Yakovlev and M. S. Wismer. Adiabatic corrections for velocity-gauge simulations of electron dynamics in periodic potentials. *Comput. Phys. Commun.* **217**, pp. 82–88 (2017).
- [67] M. S. Wismer and V. S. Yakovlev. Gauge-independent decoherence models for solids in external fields. *Phys. Rev. B* **97** no. 14, p. 144302 (2018).
- [68] J. A. Pérez-Hernández, L. Roso and L. Plaja. S-Matrix theory for the high-order harmonic generation beyond the Strong-Field Approximation. *Laser Physics* **19** no. 8, pp. 1581–1585 (2009).
- [69] E. Pisanty and M. Ivanov. Slalom in complex time: emergence of low-energy structures in tunnel ionization via complex time contours. *Phys. Rev. A* **93** no. 4, p. 043408 (2016). arXiv:1507.00011.

Supplementary Material

In this Supplementary Material (SM), we further clarify how, and under what conditions, high harmonic generation (HHG) and its circular dichroism are sensitive observables to probe topological phases and transitions in topological materials. The organization of this SM is as follows:

- In section S1, we briefly review the paradigmatic Haldane model (HM) [33], and introduce its topological invariant, the Chern Number, C .
- In section S2, we derive the time-dependent inter-band \mathbf{J}_{er} and intra-band \mathbf{J}_{ra} currents, fully considering geometrical features such as the Berry curvature $\Omega(\mathbf{k})$ and the Berry connection $\xi(\mathbf{k})$ of the system. We extend the semiconductor Bloch equations (SBEs) within the single-active electron approximation (SAE) to include geometric features in the time-evolution of the quantum-mechanical occupations and coherence.
- In section S3, we analyze the currents using the Keldysh approximation and show that this approach is gauge independent under the Bloch wavefunction calibration. We apply the saddle-point analysis to the inter-band current and discuss how the electron-hole trajectories are modified by the Berry curvature, connection and dipole moment phase
- In section S4, we discuss the dipole instabilities arising from the gauge fixing and the unphysical consequences on the harmonic spectrum. We then propose a method to avoid such discontinuities.
- In section S5, we study the linear cut-off behaviour of the HHG spectra and the relative intensities of the intra-band and inter-band contributions.
- In section S6, we expand the discussion of recent experimental measurements [26] addressed in the main text.
- In section S7, we discuss the influence of the dephasing time T_2 on the HHG spectrum, the circular dichroism and its minimum-coupling gauge independence.
- In section S8, we discuss the sensitivity of the HHG spectrum of the HM is to: (i) symmetries, i.e. time-reversal symmetry (TRS) and spatial inversion symmetry (IS), (ii) trivial and non-trivial topological phases and (iii) topological phase transitions. We also analyze, two topological phases by mean of the quasi-classical electron-hole pair trajectories to show how the topology modifies this recombination mechanism.

S1 · Haldane model

The Haldane model (HM) [33] is a prominent example of a Chern insulator with no net magnetic-flux ϕ_0 through the unit cell, as illustrated in Fig. (1) of the main text. In this section, we introduce the Hamiltonian, re-derive the eigenvalues and eigenvectors. We then introduce the Berry curvature and connection as well as the Chern number C , which is a topologically invariant quantity. Finally, we derive the relation between the Berry curvature and the dipole moment.

S1.1 · Hamiltonian

The HM is described by a tight-binding Hamiltonian of spinless fermions with a real nearest-neighbour (NN) hopping t_1 , a complex next-nearest-neighbour hopping (NNN) $t_2 e^{i\phi_0}$, and an on-site staggering potential M_0 . The Hamiltonian in momentum space reads

$$H_0(\mathbf{k}) = B_{0,\mathbf{k}} \sigma_0 + \mathbf{B}_\mathbf{k} \cdot \boldsymbol{\sigma}, \quad (\text{S1})$$

where the set of $B_{0,\mathbf{k}}$ and $\mathbf{B}_\mathbf{k} = \{B_{1,\mathbf{k}}, B_{2,\mathbf{k}}, B_{3,\mathbf{k}}\}$ are known as a “pseudomagnetic field” describing the tight-binding components of the Hamiltonian in momentum space, which read

$$\begin{aligned} B_{1,\mathbf{k}} &= t_1 \sum_{i=1}^3 \cos(\mathbf{k} \cdot \mathbf{a}_i), & B_{2,\mathbf{k}} &= t_1 \sum_{i=1}^3 \sin(\mathbf{k} \cdot \mathbf{a}_i), \\ B_{3,\mathbf{k}} &= M_0 - 2t_2 \sin \phi_0 \sum_{i=1}^3 \sin(\mathbf{k} \cdot \mathbf{b}_i), & B_{0,\mathbf{k}} &= 2t_2 \cos \phi_0 \sum_{i=1}^3 \cos(\mathbf{k} \cdot \mathbf{b}_i). \end{aligned} \quad (\text{S2})$$

Here \mathbf{a}_i are the NN vectors (from atom A to B, see Fig. 1 of the main text), $\mathbf{a}_1 = (0, a_0)$, $\mathbf{a}_2 = \left(-\frac{\sqrt{3}}{2}, -\frac{1}{2}\right) a_0$, $\mathbf{a}_3 = \left(\frac{\sqrt{3}}{2}, -\frac{1}{2}\right) a_0$ and \mathbf{b}_i are the NNN vectors (from atom A to A, or B to B) given by $\mathbf{b}_1 = (\sqrt{3}, 0) a_0$, $\mathbf{b}_2 = \left(-\frac{\sqrt{3}}{2}, +\frac{3}{2}\right) a_0$, $\mathbf{b}_3 = \left(-\frac{\sqrt{3}}{2}, -\frac{3}{2}\right) a_0$, with a_0 denoting the distance between the atoms A and B. In (S1), moreover, σ_0 is the identity matrix, and $\boldsymbol{\sigma} = \{\sigma_1, \sigma_2, \sigma_3\}$ is the vector of Pauli matrices, which is taken on a reference frame such that the eigenstates of σ_3 are Bloch waves that are localized to sites A and B, respectively, within each unit cell. The symmetries of the model are obtained as follows: (i) a non-zero magnetic flux ϕ_0 breaks the time-reversal symmetry (TRS) and (ii) a non-zero staggering potential M_0 breaks the inversion symmetry (IS).

S1.2 · Eigenvalues and eigenvectors

As the Hamiltonian is described by a 2×2 matrix in the Bloch basis, the eigenvalues and the eigenvectors of the Hamiltonian can be found analytically, using standard tools: the Hamiltonian is essentially a Pauli matrix along the $\widehat{\mathbf{B}}(\mathbf{k}) := \mathbf{B}_\mathbf{k} / |\mathbf{B}_\mathbf{k}|$ direction in the same space as the σ Pauli vector, and its eigenvectors are the corresponding spin states as usual.

The energy spectrum thus reads

$$\varepsilon_{c/v}(\mathbf{k}) = B_{0,\mathbf{k}} \pm |\mathbf{B}_\mathbf{k}|, \quad (\text{S3})$$

with the upper (lower) sign corresponding to the conduction (valence) band. We define also, for future use, the polar coordinates $\phi_\mathbf{k}$ and $\theta_\mathbf{k}$ of $\widehat{\mathbf{B}}(\mathbf{k})$, as $\tan \phi_\mathbf{k} := \frac{\widehat{B}_{2,\mathbf{k}}}{\widehat{B}_{1,\mathbf{k}}}$ and $\cos \theta_\mathbf{k} := \widehat{B}_{3,\mathbf{k}}$. The eigenvectors of H_0 at crystal momentum \mathbf{k} are given, in this language, by

$$|u_{+,\mathbf{k}}\rangle = \frac{1}{N_{+,\mathbf{k}}} \begin{pmatrix} B_{3,\mathbf{k}} + |\mathbf{B}_\mathbf{k}| \\ B_{1,\mathbf{k}} + iB_{2,\mathbf{k}} \end{pmatrix} = \begin{pmatrix} e^{-i\phi_\mathbf{k}/2} \cos \frac{\theta_\mathbf{k}}{2} \\ e^{+i\phi_\mathbf{k}/2} \sin \frac{\theta_\mathbf{k}}{2} \end{pmatrix}, \quad (\text{S4})$$

$$|u_{-,\mathbf{k}}\rangle = \frac{1}{N_{-,\mathbf{k}}} \begin{pmatrix} iB_{2,\mathbf{k}} - B_{1,\mathbf{k}} \\ B_{3,\mathbf{k}} + |\mathbf{B}_\mathbf{k}| \end{pmatrix} = \begin{pmatrix} e^{-i\phi_\mathbf{k}/2} \sin \frac{\theta_\mathbf{k}}{2} \\ -e^{+i\phi_\mathbf{k}/2} \cos \frac{\theta_\mathbf{k}}{2} \end{pmatrix}, \quad (\text{S5})$$

with $N_{\pm,\mathbf{k}}$ a suitable normalization constant. As usual, these eigenstates are only defined up to a (possibly \mathbf{k} -dependent) phase, changes to which are the Bloch gauge transformations that we will examine in depth in section S4. A gauge transformation of the wavefunction (S5) can be performed by an unitary transformation and would lead to a new vector $\mathbf{B}'_\mathbf{k} = \{B'_{1,\mathbf{k}}, B'_{2,\mathbf{k}}, B'_{3,\mathbf{k}}\}$ (for example $\mathbf{B}' = \{B_2, B_3, B_1\}$). Such transformation keeps invariant the energy dispersions and Berry curvatures but modifies ξ_m and $\mathbf{d}_{m,m'}$. This gauge control will be implemented numerically to manipulate the discontinuities and singularities of the dipole matrix element and Berry connections in the BZ of topological phases.

S1.3 · Berry Connection, Curvature and Chern number

We now turn to the relation between the the dipole matrix element and the Berry connection. To this end, we explicitly compute the Berry connection introduced in Eq. (S15) and fix the gauge as in the right-hand side of Eq. (S5); in these terms, the Berry connection reads

$$\xi_{v/c}(\mathbf{k}) = \mp \frac{1}{2} (\cos \theta_\mathbf{k}) (\nabla_\mathbf{k} \phi_\mathbf{k}). \quad (\text{S6})$$

The Berry curvature can therefore be written as

$$\Omega_{v/c}(\mathbf{k}) = \nabla_\mathbf{k} \times \xi_{v/c}(\mathbf{k}) = \mp \frac{1}{2} (\nabla_\mathbf{k} \cos \theta_\mathbf{k}) \times (\nabla_\mathbf{k} \phi_\mathbf{k}), \quad (\text{S7})$$

and the topological invariant, the Chern number, can be calculated as the integral over the BZ of the Berry curvature

$$C_{c/v} = \mp \frac{1}{4\pi} \int_{\text{BZ}} d^2\mathbf{k} \cdot [\sin \theta_\mathbf{k} (\nabla_\mathbf{k} \theta_\mathbf{k}) \times (\nabla_\mathbf{k} \phi_\mathbf{k})]. \quad (\text{S8})$$

In the HM, the Chern number of the conduction band $C_c = C$ can take the values of -1 , 0 and $+1$ depending on M_0 and ϕ_0 , see Fig. (1) of main text. The trivial phase has a zero Chern number and the two topological phases are characterized by Chern numbers $C = \pm 1$.

S1.4 · Dipole moment and the Berry curvature in the Haldane model

We now turn to the dipole matrix element, as initially defined in Eq. (S14), and which is here given by

$$\mathbf{d}_{cv}(\mathbf{k}) = \frac{1}{2} [(\sin \theta_\mathbf{k}) (\nabla_\mathbf{k} \phi_\mathbf{k}) + i \nabla_\mathbf{k} \theta_\mathbf{k}]. \quad (\text{S9})$$

On the one hand, we find that the cross product of the HM dipole Eq. (S9) yields

$$\text{Im}(d_{cv}^x d_{cv}^{y*}) = \frac{1}{4} \sin \theta_\mathbf{k} [\partial_{k_y} \theta_\mathbf{k} \partial_{k_x} \phi_\mathbf{k} - \partial_{k_x} \theta_\mathbf{k} \partial_{k_y} \phi_\mathbf{k}]. \quad (\text{S10})$$

And expanding the Berry curvature in the HM given by Eq. (S7), one obtains

$$\begin{aligned} \Omega_{v/c}(\mathbf{k}) &= \mp \frac{1}{2} \sin \theta_\mathbf{k} (\nabla_\mathbf{k} \theta_\mathbf{k} \times \nabla_\mathbf{k} \phi_\mathbf{k}) \\ &= \mp \frac{1}{2} \sin \theta_\mathbf{k} [\partial_{k_y} \theta_\mathbf{k} \partial_{k_x} \phi_\mathbf{k} - \partial_{k_x} \theta_\mathbf{k} \partial_{k_y} \phi_\mathbf{k}]. \end{aligned} \quad (\text{S11})$$

We conclude, thus, that $\Omega_{v/c} = \mp 2 \text{Im}[d_{cv}^{(x)} d_{cv}^{*(y)}]$, which demonstrates the close relationship between dipole matrix elements and the Berry curvature in the HM. This confirmation of the relation of the dipole product with the Berry curvature is extremely important, since this leads to a direct connection of the inter-band transition current of Eq. (S24) and the topological invariant for this model.

S2 · Semiconductor Bloch equations, the geometry and topology of the energy bands

Here we introduce and derive the microscopic time-dependent response of laser-solid-matter interaction.

S2.1 · Microscopic currents

We here derive the total microscopic current $\mathbf{J}(t) = \mathbf{J}_{\text{ra}}(t) + \mathbf{J}_{\text{er}}(t)$, by focusing on its two components: the intra-band $\mathbf{J}_{\text{ra}}(t)$ and the inter-band $\mathbf{J}_{\text{er}}(t)$ currents [17, 18]. To this end, we study the dynamics of the time-dependent wavefunction $|\Psi(t)\rangle = \sum_m \int_{\text{BZ}} d\mathbf{k} a_m(\mathbf{k}, t) |\Phi_{m,\mathbf{k}}\rangle$, written as a linear combination of Bloch states $|\Phi_{m,\mathbf{k}}\rangle$ where $m = v, c$ denotes the valence and conduction bands respectively (for simplicity, we restrict ourselves to a two-band model) and where $a_m(\mathbf{k}, t)$ is defined as the probability amplitude of the valence or conduction band.

S2.1.1 · Inter-band current

We first write the inter-band current $\mathbf{J}_{\text{er}}(t) = \frac{d}{dt} \mathbf{P}_{\text{er}}(t)$ in terms of the polarization

$$\mathbf{P}_{\text{er}}(t) \equiv e \langle \Psi(t) | \mathbf{x} | \Psi(t) \rangle = e \int_{\text{BZ}'} d\mathbf{k}' \int_{\text{BZ}} d\mathbf{k} a_c(\mathbf{k}', t) a_v^*(\mathbf{k}, t) \langle \Phi_{v,\mathbf{k}'} | \mathbf{x} | \Phi_{c,\mathbf{k}} \rangle + \text{c.c.}, \quad (\text{S12})$$

where $e = -1$ a.u. is the electron's charge. We follow Blount [61] to evaluate the polarization with the help of the identity

$$\langle \Phi_{m',\mathbf{k}'} | \mathbf{x} | \Phi_{m,\mathbf{k}} \rangle = -i \nabla_{\mathbf{k}} (\delta_{m'm} \delta(\mathbf{k} - \mathbf{k}')) + \delta(\mathbf{k} - \mathbf{k}') \mathbf{d}_{m'm}(\mathbf{k}), \quad (\text{S13})$$

where the indices m, m' stand for valence and conduction bands, $\delta_{m'm}$ and $\delta(\mathbf{k} - \mathbf{k}')$ are the Kronecker and Dirac deltas, respectively, \mathbf{x} is the position operator in the crystal,

$$\mathbf{d}_{m'm}(\mathbf{k}) = i \langle u_{m',\mathbf{k}} | \nabla_{\mathbf{k}} | u_{m,\mathbf{k}} \rangle, \quad (\text{S14})$$

is the dipole matrix element for $m \neq m'$, which is defined in terms of the periodic part of the m^{th} Bloch state $|u_{m,\mathbf{k}}\rangle$ and

$$\begin{aligned} \xi_m(\mathbf{k}) &= \mathbf{d}_{mm}(\mathbf{k}) \\ &= i \langle u_{m,\mathbf{k}} | \nabla_{\mathbf{k}} | u_{m,\mathbf{k}} \rangle, \end{aligned} \quad (\text{S15})$$

is the Berry connection [61]. We therefore find

$$\mathbf{J}_{\text{er}}(t) = e \frac{d}{dt} \int_{\overline{\text{BZ}}} \mathbf{d}_{cv}^* (\mathbf{K} + \mathbf{A}(t)) \pi(\mathbf{K}, t) d^3 \mathbf{K} + \text{c.c.}, \quad (\text{S16})$$

where $\pi(\mathbf{k}, t) = a_v^*(\mathbf{k}, t) a_c(\mathbf{k}, t)$ is the population coherence (see Sec. S2.2 for details) and the momentum integral is performed over the Brillouin zone $\overline{\text{BZ}} = \text{BZ} - \mathbf{A}(t)$ shifted by the laser-field vector potential $\mathbf{A}(t)$. Here $\mathbf{K} = \mathbf{k} - \mathbf{A}(t)$ is the quasi-canonical momentum defined in terms of the electron crystal momentum \mathbf{k} and the vector potential $\mathbf{A}(t)$ of the electric laser field $\mathbf{E}(t) = -\partial_t \mathbf{A}(t)$. This result coincides with the ones found by Vampa *et al.* in Ref. [58].

S2.1.2 · Intra-band current

We write the intra-band current $\mathbf{J}_{\text{ra}}(t) = e \sum_m \langle \Psi(t) | \mathbf{v}_m | \Psi(t) \rangle$ in terms of the intra-band velocity operator $\mathbf{v}_m = -i[x_m, H_0] - i[x_m, \mathbf{x}_m \cdot \mathbf{E}(t)]$. We use the electromagnetic length gague with the single-active-electron Hamiltonian and the dipole approximation of the laser-crystal system, i.e. $H(t) = H_0 + \mathbf{x} \cdot \mathbf{E}(t)$. For simplicity, our derivation is focused on the conduction band $m = c$ of the intra-band current, which reads

$$\begin{aligned} \mathbf{J}_{\text{ra}}(t) &= e \int d\mathbf{k}' \int d\mathbf{k} a_{c,\mathbf{k}'}^*(t) a_{c,\mathbf{k}}(t) \langle \Phi_{c,\mathbf{k}'} | \mathbf{x}_c | \Phi_{c,\mathbf{k}} \rangle \varepsilon_c(\mathbf{k}) + (c \rightarrow v) \\ &= e \int d\mathbf{k}' [n_c(\mathbf{k}', t) \mathbf{v}_c(\mathbf{k}') + n_v(\mathbf{k}', t) \mathbf{v}_v(\mathbf{k}')]. \end{aligned} \quad (\text{S17})$$

Here, $n_c(\mathbf{k}, t) = a_c^*(\mathbf{k}, t) a_c(\mathbf{k}, t)$ is the population and $\mathbf{v}_c(\mathbf{k}) = \mathbf{v}_{\text{gr},c}(\mathbf{k}) + \mathbf{v}_{a,c}(\mathbf{k})$ is written in terms of the group velocity $\mathbf{v}_{\text{gr},c}(\mathbf{k}) = \nabla_{\mathbf{k}} \varepsilon_c(\mathbf{k})$, and the anomalous velocity $\mathbf{v}_{a,c}(\mathbf{k}) = -\mathbf{E}(t) \times \boldsymbol{\Omega}_c(\mathbf{k})$, where $\boldsymbol{\Omega}_m(\mathbf{k}) = \nabla_{\mathbf{k}} \times \xi_m(\mathbf{k})$ is the Berry curvature. The anomalous-velocity term comes from considering that the intra-band component $x_m^{(j)}$ of the position operator does not commute with $x_m^{(i)}$ component (see Ref. 61). The indices i and j stand for the x, y and z components of the operator \mathbf{x} . This intra-band current also can be expressed on the shifted Brillouin zone $\overline{\text{BZ}}$, as

$$\mathbf{J}_{\text{ra}}(t) = e \sum_m \int_{\overline{\text{BZ}}} \mathbf{v}_m (\mathbf{K} + \mathbf{A}(t)) n_m(\mathbf{K}, t) d^3 \mathbf{K}. \quad (\text{S18})$$

In order to calculate the HHG spectrum from a crystal, we have to evaluate Eqs. (S16) and (S18). Hence, our main task in the following will be to compute the coherence $\pi(\mathbf{k}, t)$ and the occupations $n_m(\mathbf{k}, t)$, which are related to the transition amplitude $a_m(\mathbf{k}, t)$.

In our numerical calculations we compute the radiated power on each harmonic frequency by coherently superposing the time derivatives of the intra- and inter-band currents, and then taking the squared modulus of its Fourier transform, i.e. $I_{\text{HHG}}(\omega) = \omega^2 |\text{FT} [\mathbf{J}_{\text{er}}(t) + \mathbf{J}_{\text{ra}}(t)]|^2$.

S2.2 · Semiconductor Bloch equations

The time evolution of the probability amplitudes $a_m(\mathbf{k}, t)$ can be computed with the help of the Schrödinger equation which results in [61]

$$i\dot{a}_m(\mathbf{k}', t) = \varepsilon_m(\mathbf{k}') a_m(\mathbf{k}', t) + \mathbf{E}(t) \cdot \sum_{m'} \int_{\text{BZ}} \langle \Phi_{m, \mathbf{k}'} | \mathbf{x} | \Phi_{m', \mathbf{k}} \rangle a_{m'}(\mathbf{k}', t).$$

Here $\varepsilon_m(\mathbf{k})$ denotes the energy dispersion for the valence/conduction band v/c ($m = v$), and m' also ranges over both bands. We then compute the second and third terms on the right-hand side of above equation by using Eq. (S13), and we find

$$\dot{a}_m(\mathbf{k}, t) = -i [\varepsilon_m(\mathbf{k}) + \mathbf{E}(t) \cdot \boldsymbol{\xi}_m(\mathbf{k}) + i\mathbf{E}(t) \cdot \nabla_{\mathbf{k}}] a_m(\mathbf{k}, t) - i\mathbf{E}(t) \cdot \sum_{m' \neq m} \mathbf{d}_{mm'}(\mathbf{k}) a_{m'}(\mathbf{k}, t). \quad (\text{S19})$$

We now work with the shifted Brillouin zone $\overline{\text{BZ}}$, which will allow us to remove the gradient $\nabla_{\mathbf{k}}$ from Eq. (S19) (see Ref. 58 for more details). This is done by the substitution $a_m(\mathbf{k}, t) = e^{\mathbf{A}(t) \cdot \nabla_{\mathbf{k}}} b_m(\mathbf{K}, t)$ and one finds

$$\dot{b}_m(\mathbf{K}, t) = -i [\varepsilon_m(\mathbf{K} + \mathbf{A}(t)) + \mathbf{E}(t) \cdot \boldsymbol{\xi}_m(\mathbf{K} + \mathbf{A}(t))] b_m(\mathbf{K}, t) - i\mathbf{E}(t) \cdot \sum_{m' \neq m} \mathbf{d}_{mm'}(\mathbf{K} + \mathbf{A}(t)) b_{m'}(\mathbf{K}, t), \quad (\text{S20})$$

where $\mathbf{K} = \mathbf{k} - \mathbf{A}(t)$ is the quasi-crystal canonical momentum. We transform the transition amplitude b_m to the density matrix operator $\hat{\rho}$, i.e. the population $n_m = \rho_{mm}$ and coherence $\pi = \rho_{mm'}$, $m \neq m'$, $n_m(\mathbf{K}, t) = b_m^*(\mathbf{K}, t) b_m(\mathbf{K}, t)$, and $\pi(\mathbf{K}, t) = b_c(\mathbf{K}, t) b_v^*(\mathbf{K}, t)$. Thus, this leads to the so-called semiconductor Bloch equations (SBEs, in the moving frame \mathbf{K}), which describe the laser-electron interaction in the lattice [23], and in particular the electron-hole dynamics of the crystal target. We obtain the next couple of equations of motion for the population and coherence:

$$\dot{n}_m(\mathbf{K}, t) = i(-1)^m \mathbf{E}(t) \cdot \mathbf{d}_{cv}^*(\mathbf{K} + \mathbf{A}(t)) \pi(\mathbf{K}, t) + \text{c.c.}, \quad (\text{S21})$$

$$\dot{\pi}(\mathbf{K}, t) = -i \left[\varepsilon_g(\mathbf{K} + \mathbf{A}(t)) + \mathbf{E}(t) \cdot \boldsymbol{\xi}_g(\mathbf{K} + \mathbf{A}(t)) - i\frac{1}{T_2} \right] \pi(\mathbf{K}, t) - i\mathbf{E}(t) \cdot \mathbf{d}_{cv}(\mathbf{K} + \mathbf{A}(t)) w(\mathbf{K}, t). \quad (\text{S22})$$

Here $\varepsilon_g(\mathbf{k}) = \varepsilon_c(\mathbf{k}) - \varepsilon_v(\mathbf{k})$ is the energy gap between the conduction and valence bands, as a function of the crystal momentum \mathbf{k} , $\boldsymbol{\xi}_g(\mathbf{k}) = \boldsymbol{\xi}_c(\mathbf{k}) - \boldsymbol{\xi}_v(\mathbf{k})$ is the difference in the Berry connection between the conduction and valence bands, and the sign $(-1)^m$ takes the values $(-1)^c = 1$ and $(-1)^v = -1$. We also introduce a phenomenological dephasing term written in terms of the dephasing time T_2 [18]. Finally, $w(\mathbf{k}, t) = n_v(\mathbf{k}, t) - n_c(\mathbf{k}, t)$ denotes the momentum-time dependent of the population difference between the valence- and conduction-band or inversion population. In our calculations, we describe the driving laser using the vector potential

$$\mathbf{A}(t) = \frac{E_0}{\omega_0} f(t) \left(\frac{1}{\sqrt{1+\epsilon^2}} \cos(\omega_0(t-t_0) - \varphi_{\text{CEP}}) \mathbf{e}_x + \frac{\epsilon}{\sqrt{1+\epsilon^2}} \sin(\omega_0(t-t_0) - \varphi_{\text{CEP}}) \mathbf{e}_y \right), \quad (\text{S23})$$

where E_0 is the laser field strength, ω_0 the central photon frequency, $\varphi_{\text{CEP}} = 0$ is the carrier-envelope phase, and $f(t)$ is the laser-pulse envelope, given by $f(t) = \exp((t-t_0)^2/(2\sigma^2))$, where σ is the pulse width. Here, \mathbf{e}_x denotes the unitary vector along the x direction and ϵ denotes the ellipticity of the laser, given by $\epsilon = -1$ (+1) for right-handed (left-handed) circularly polarized (RCP, LCP, resp.) laser fields, and by $\epsilon = 0$ for linearly-polarized laser drivers. The electric field is given by the negative of the time-derivative of (S23), i.e. $\mathbf{E}(t) = -\partial_t \mathbf{A}(t)$. We numerically solve the SBEs described in Eqs. (S21) and (S22) with a 5th-order Runge–Kutta scheme, implemented in C++ using the Message Passing Interface (MPI) to parallelize the computations. Additionally, we validate our numerical findings in C++ comparing our numerical outcomes with the numerical solution by the built-in solvers on Wolfram *Mathematica*. We find very good agreement between the C++ and *Mathematica* results.

S3 · Inter-band and intra-band mechanisms in topological materials

We focus our attention on the Keldysh approximation, in analogy to that introduced by Vampa *et al.* [58], and analyze the inter-band contribution to the HHG emission. This approximation in a crystal solid reads as $w(\mathbf{k}, t) = n_v(\mathbf{k}, t) - n_c(\mathbf{k}, t) \approx 1$. Basically, this means that the population transferred to the conduction band is very small compared to the remaining one in the valence band. In the following we will call it the Strong Field Approximation (SFA) for the laser-topological material model.

S3.1 · Inter-band current

We decouple Eq. (S21) from Eq. (S22) by considering the Keldysh approach and obtain for i^{th} vectorial-component $i = x, y, z$, of inter-band current contribution,

$$J_{\text{ef}}^{(i)}(t) = -i \sum_j \frac{d}{dt} \int_{t_0}^t dt' \int_{\overline{\text{BZ}}} d^3\mathbf{K} \left| d_{cv}^{(i)}(\mathbf{K} + \mathbf{A}(t)) \right| \times \left| d_{cv}^{(j)}(\mathbf{K} + \mathbf{A}(t')) \right| E^{(j)}(t') \\ \times e^{-iS(\mathbf{K}, t, t') - (t-t')/T_2 + i(\phi_{cv}^{(j)}(\mathbf{K}, t) - \phi_{cv}^{(i)}(\mathbf{K}, t))} + \text{c.c.}, \quad (\text{S24})$$

where $S(\mathbf{K}, t, t')$ is the so-called quasi-classical action for the electron-hole, which is defined as

$$S(\mathbf{K}, t, t') = \int_{t'}^t \left[\varepsilon_g(\mathbf{K} + \mathbf{A}(t'')) + \mathbf{E}(t'') \cdot \boldsymbol{\xi}_g(\mathbf{K} + \mathbf{A}(t'')) - \frac{d}{dt''} \phi_{cv}^{(j)}(\mathbf{K} + \mathbf{A}(t'')) \right] dt''. \quad (\text{S25})$$

Here j determines the component of the electric field and dipole phase. This index stands for the laser field components, x , y or z , depending on the polarization state of the driving laser. Note that the dipole phase in the action has the same index as the electric field j and the additional term $\phi_{cv}^{(j)}(t) - \phi_{cv}^{(i)}(t)$ only contributes in the perpendicular-emission configuration $i \neq j$, if one assumes the laser field is linearly polarized along the x direction.

This integral form of the inter-band current has a nice physical interpretation: (i) at time t' the electron-hole is excited by the driving laser from the valence band to the conduction band through the dipolar interaction $\mathbf{d}_{cv}(\mathbf{K} + \mathbf{A}(t')) \cdot \mathbf{E}(t')$ at the quasi-canonical crystal momentum \mathbf{K} ; (ii) the electron (hole) propagates in the conduction (valence) band between t' and t , and modify their trajectories and energies according to Eq. (S25); and (iii) at time t the electron has a probability to recombine (or annihilate) with the hole, at which point it emits its excess energy as a high energy-photon.

S3.2 · Gauge transformation of the dipole and Berry connection

The formula for the inter-band current, Eq. (S24) is gauge invariant including the semi-classical action in Eq. (S25). In order to show this, in the following we will address the behaviour of the dipole and the Berry connection under a gauge transformation. Under the gauge transformation $|u_{m,\mathbf{k}}\rangle \Rightarrow e^{-i\varphi_m(\mathbf{k})}|u_{m,\mathbf{k}}\rangle$ [see Eq. (2.5) of Ref. 61], the dipole matrix element $\mathbf{d}_{cv}(\mathbf{k})$ transforms as

$$\tilde{\mathbf{d}}_{cv}(\mathbf{k}) = e^{i\varphi_c(\mathbf{k})}\mathbf{d}_{cv}(\mathbf{k})e^{-i\varphi_v(\mathbf{k})}.$$

The vector components of the dipole $\mathbf{d}_{cv}(\mathbf{k})$ can be written in terms of their complex amplitude and phase, $d_{cv}^{(i)}(\mathbf{k}) = |d_{cv}^{(i)}(\mathbf{k})|e^{-i\phi_{cv}^{(i)}(\mathbf{k})}$. Here, the index i stands for the x , y and z components of the dipole $\mathbf{d}_{cv}(\mathbf{k})$. In that case, we obtain

$$\tilde{d}_{cv}^{(i)}(\mathbf{k}) = |d_{cv}^{(i)}(\mathbf{k})|e^{-i(\phi_{cv}^{(i)}(\mathbf{k}) - \varphi_g(\mathbf{k}))}.$$

If the same argument of dipole amplitude and phase is applied to the new dipole $\tilde{d}_{cv}^{(i)}(\mathbf{k}) = |\tilde{d}_{cv}^{(i)}(\mathbf{k})|e^{-i\tilde{\phi}_{cv}^{(i)}(\mathbf{k})}$, then the gauge transformation for new dipole transition moment's phase reads

$$\tilde{\phi}_{cv}^{(i)}(\mathbf{k}) = \phi_{cv}^{(i)}(\mathbf{k}) - \varphi_g(\mathbf{k}), \quad (\text{S26})$$

where $\varphi_g = \varphi_c - \varphi_v$ is the wavefunction gauge calibration difference. Note, here, that the amplitude of the dipole matrix element $|\tilde{\mathbf{d}}_{cv}(\mathbf{k})| = |\mathbf{d}_{cv}(\mathbf{k})|$ is unaffected. Therefore, we would expect the dipole matrix transition amplitude to be a gauge-invariant quantity, but its phase is gauge dependent and transforms according to Eq. (S26).

The Berry connection, on the other hand, transforms as

$$\tilde{\xi}_m(\mathbf{k}) = \xi_m(\mathbf{k}) + \nabla_{\mathbf{k}}\varphi_m(\mathbf{k}), \quad (\text{S27})$$

under that same gauge transformation [61], with φ_m the wave function phase of the m^{th} band in the new gauge. Once we define the gauge transformation rules for the connection and the phases of the dipole matrix elements, we proceed to find a general invariant phase for the inter-band current and its associated semi-classical action.

S3.3 · Relationship between the Berry curvature and the dipole matrix elements

In this section, we demonstrate the general relation between the Berry curvature and the dipole matrix element. As it is introduced in Section 1.1, the Berry curvature is defined as the curl of the Berry connection, which can be expanded as

$$\Omega_m(\mathbf{k}) = i \langle \nabla_{\mathbf{k}} u_{m,\mathbf{k}} | \times | \nabla_{\mathbf{k}} u_{m,\mathbf{k}} \rangle.$$

By using the identity operator $\sum_{m'}^N |u_{m',\mathbf{k}}\rangle\langle u_{m',\mathbf{k}}| = 1$, we can write explicitly the Berry curvature as (see Ref. [61]),

$$\Omega_m(\mathbf{k}) = i \sum_{m' \neq m} \mathbf{d}_{m,m'}(\mathbf{k}) \times \mathbf{d}_{m',m}(\mathbf{k}). \quad (\text{S28})$$

For 2D materials, an straight forward relationship between the Berry curvature and the transition dipole matrix element can easily be found:

$$\hat{\mathbf{z}} \cdot \boldsymbol{\Omega}_m(\mathbf{k}) = 2 \operatorname{Im} \left[\sum_{m' \neq m} d_{m,m'}^{(x)}(\mathbf{k}) d_{m',m}^{(y)}(\mathbf{k}) \right]. \quad (\text{S29})$$

This analytical finding is extremely important. Since the inter-band current along the orthogonal emission to the driving field will contain a cross product between dipole matrix elements along the x and y directions (and, of course, the integral of the inter-band current is performed over the whole BZ), this means that the topological invariant – the Chern number – should be encoded in this transverse harmonic-emission component. This property will play an important role in the relationship between the harmonic emission and the topological invariant, in particular for interband current, see Sec. 3.5.

S3.3.1 · Quasi-classical action

Then, let us try in order to demonstrate whether the action phase (S25) is gauge invariant or not. The action phase \tilde{S} can be written as

$$\tilde{S}(\mathbf{K}, t, t') = \int_{t'}^t \left[\tilde{\varepsilon}_g(\mathbf{K} + \mathbf{A}(t'')) + \mathbf{E}(t'') \cdot \tilde{\xi}_g(\mathbf{K} + \mathbf{A}(t'')) - \frac{d}{dt''} \tilde{\phi}_{cv}^{(j)}(\mathbf{K} + \mathbf{A}(t'')) \right] dt'', \quad (\text{S30})$$

where $\tilde{\varepsilon}_g = \varepsilon_g$ is gauge invariant, but $\tilde{\xi}_g$ and $\tilde{\phi}_{cv}^{(j)}$ are not. However, we can use the transformation rules (S26) and (S27), for the dipole phase and the Berry connection:

$$\tilde{S}(\mathbf{K}, t, t') = \int_{t'}^t \left[\varepsilon_g + \mathbf{E}(t'') \cdot (\xi_g + \nabla_{\mathbf{K}} \varphi_g) - \frac{d}{dt''} (\phi_{cv}^{(j)} - \varphi_g) \right] dt''.$$

(For simplicity, we drop the dependence on the variable $\mathbf{K} + \mathbf{A}(t)$). Moreover, by using the fact that $-\mathbf{E}(t) \cdot \nabla_{\mathbf{k}} = \frac{d}{dt}$ and in addition $\nabla_{\mathbf{k}} = \nabla_{\mathbf{K}}$ [5], we have $(\mathbf{E}(t'') \cdot \nabla_{\mathbf{K}} + \frac{d}{dt''}) \varphi_g = 0$, which leads finally to the relation

$$\tilde{S}(\mathbf{K}, t, t') = \int_{t'}^t \left[\varepsilon_g + \mathbf{E}(t'') \cdot \xi_g - \frac{d}{dt''} \phi_{cv}^{(j)} \right] dt''.$$

Since the latter expression is equal to Eq. (S25), we find that $S(\mathbf{K}, t, t')$ is gauge invariant. Furthermore, as the HHG spectrum is an experimental observable, the currents should be gauge-invariant quantities. Our analysis here shows that this is still the case for our theoretical model. Here, we show a gauge-invariant action even in the presence of a nontrivial Berry connection. In addition, we can also rewrite the semiclassical action as

$$S(\mathbf{K}, t, t') = \int_{t'}^t \left[\varepsilon_g(\mathbf{K} + \mathbf{A}(t'')) + \mathbf{E}(t'') \cdot (\xi_g(\mathbf{K} + \mathbf{A}(t'')) + \nabla_{\mathbf{K}} \phi_{cv}^{(j)}(\mathbf{K} + \mathbf{A}(t''))) \right] dt'', \quad (\text{S31})$$

by explicitly calculating the time derivative of the dipole phase, $\frac{d}{dt''} \phi_{cv}^{(j)}$, to bring to the for the explicit factor of the electric field, $\mathbf{E}(t'')$. Here the action phase includes geometric and topological properties, such as the Berry connection and the dipole phase $\phi_{vc}^{(j)}(\mathbf{k})$. Given this form, it is probable that the electron-hole pair trajectories will be modified by these geometric properties, thereby affecting the non-linear HHG process. The total phase of Eq. (S24) has an extra dipole-phase contribution, $\phi_{cv}^{(i)} - \phi_{cv}^{(j)}$ regarding the “perpendicular” inter-band current to the electric field. From the phase transformation given by Eq. (S26), this phase difference term is also gauge invariant.

S3.4 · Quasi-classical approach and electron-hole pair trajectories

Assuming that the exponentiated quasi-classical action $e^{-iS} = e^{-iS(\mathbf{K}, t, t')}$ oscillates rapidly as a function of the crystal momentum \mathbf{K} , one can apply the saddle point approximation to find the points \mathbf{K}_s where the integrand's contributions to the inter-band current (S24) concentrate. These are solutions of the saddle-point equation $\nabla_{\mathbf{K}} S(\mathbf{K}, t, t')|_{\mathbf{K}_s} = \mathbf{0}$, which can be rephrased as

$$\Delta \mathbf{x}_c(\mathbf{K}_s, t, t') - \Delta \mathbf{x}_v(\mathbf{K}_s, t, t') = \mathbf{0}. \quad (\text{S32})$$

From the last equation two different trajectories are identified, the first one related to the excited electron $\Delta \mathbf{x}_c(\mathbf{K}_s, t, t')$ in the conduction band, and the second one regarding the trajectory $\Delta \mathbf{x}_v(\mathbf{K}_s, t, t')$ followed by the hole in the valence band. We then obtain a general m^{th} trajectory for the electron ($m = c$) and hole ($m = v$), which reads

$$\Delta \mathbf{x}_m(\mathbf{K}_s, t, t') = \int_{t'}^t \left[\mathbf{v}_{\text{gr},m} + (\mathbf{E}(t'') \cdot \nabla_{\mathbf{K}}) \left(\xi_m + (-1)^m \frac{1}{2} \nabla_{\mathbf{K}} \phi_{cv}^{(j)} \right) + \mathbf{E}(t'') \times \boldsymbol{\Omega}_m \right] dt'', \quad (\text{S33})$$

where $(-1)^m$ is the alternating sign $(-1)^c = +1$ and $(-1)^v = -1$, and the m^{th} band's group velocity is $\mathbf{v}_{\text{gr},m} = \nabla_{\mathbf{K}}\varepsilon_m$. Here we recognize the Berry curvature $\boldsymbol{\Omega}_m$ as well as the anomalous velocity $\mathbf{v}_{a,m}$, which are given by $\boldsymbol{\Omega}_m = \nabla_{\mathbf{K}} \times \boldsymbol{\xi}_m$ and $\mathbf{v}_{a,m} = \mathbf{E}(t) \times \boldsymbol{\Omega}_m$, respectively, for the electron-hole trajectories of Eq. (S33). We can rewrite the previous expression as

$$\Delta \mathbf{x}_m(\mathbf{K}_s, t, t') = \int_{t'}^t \left[\mathbf{v}_{\text{gr},m} - \frac{d}{dt''} \left(\boldsymbol{\xi}_m + \frac{(-1)^m}{2} \nabla_{\mathbf{K}} \phi_{cv}^{(j)} \right) + \mathbf{v}_{a,m} \right] dt''. \quad (\text{S34})$$

These electron-hole pair trajectories, together with the saddle-point condition of Eq. (S32), should produce complex-valued solutions for \mathbf{K}_s , as in HHG from gases. However, finding the solutions \mathbf{K}_s is not a trivial task, since it depends explicitly on the geometrical features, i.e. Berry curvature, connection, and the phase of the dipole matrix elements. Nevertheless, these saddle points \mathbf{K}_s should have a component perpendicular to driving laser field $\mathbf{E}(t)$ in case of linear drivers; this appears as a consequence of anomalous-velocity features, and in particular of the Berry curvature $\boldsymbol{\Omega}_m(\mathbf{k})$.

S3.4.1 · Electron-hole creation

To investigate the corresponding electron-hole pair birth time t'_s and determine its “nature” (real or complex), we apply the saddle-point approximation to look for the excitation/creation time t' , as $\partial_{t'} S(\mathbf{K}, t, t') = 0$, to the inter-band current Eq. (S24), which reads

$$\varepsilon_g(\mathbf{K} + \mathbf{A}(t')) + \mathbf{E}(t') \cdot \left(\boldsymbol{\xi}_g(\mathbf{K} + \mathbf{A}(t')) + \nabla_{\mathbf{K}} \phi_{cv}^{(j)}(\mathbf{K} + \mathbf{A}(t')) \right) = 0. \quad (\text{S35})$$

The electron-hole energy difference ε_g should then be the same as the negative of the coupling energy between the Berry connection (or, more specifically, a difference in $\boldsymbol{\xi}_g$ between the bands) and the driving laser field at time t' . In addition, we note that there exists the possibility to find a real (or, more generally, complex) solution for t'_s that satisfies the latter formula for the electron-hole creation. Hence, the saddle-point birth time t'_s should be a complex quantity in general, according to this saddle point approximation. We might conclude that the electron-hole creation process is a tunneling excitation one, which takes place at the same momentum \mathbf{K} .

S3.4.2 · Electron-hole annihilation

Considering the Fourier transform of the inter-band current of Eq. (S24), we can easily obtain

$$J_{\text{er}}^{(i)}(\omega) = \omega \sum_j \int_{-\infty}^{+\infty} dt \int_{t_0}^t dt' \int_{\overline{\text{BZ}}} d^3 \mathbf{K} |d_{cv}^{(i)}(\mathbf{K} + \mathbf{A}(t))| |d_{cv}^{(j)}(\mathbf{K} + \mathbf{A}(t'))| |E^{(j)}(t')| \\ \times e^{-i[S(\mathbf{K}, t, t') - \omega t] - (t-t')/T_2 + i(\phi_{cv}^{(j)}(\mathbf{K}, t) - \phi_{cv}^{(i)}(\mathbf{K}, t))} + \text{c.c.} \quad (\text{S36})$$

If one is interested in knowing what would be the photon-energy emission ω , a good approximation is also given by a saddle-point at the so called recombination or annihilation time t , $\partial_t [S(\mathbf{K}, t, t') - \omega t] = 0$, which reads,

$$\omega = \varepsilon_g(\mathbf{K} + \mathbf{A}(t)) + \mathbf{E}(t) \cdot \left(\boldsymbol{\xi}_g(\mathbf{K} + \mathbf{A}(t)) + \nabla_{\mathbf{K}} \phi_{cv}^{(j)}(\mathbf{K} + \mathbf{A}(t)) \right). \quad (\text{S37})$$

Here we recognize that the electron-hole is annihilated at the time t , with the emission of its accumulated energy into a photon of energy $\hbar\omega_0$.

S3.5 · Topology and inter-band current

In the limit of a 2D material, the description of a Chern insulator driven by a linearly- (or circularly-)polarized laser field, the inter-band current for the orthogonal component to this driving laser reads

$$J_{\text{er}}^{(y)}(t) = -i \frac{d}{dt} \int_{t_0}^t dt' \int_{\overline{\text{BZ}}} d^2 \mathbf{K} D^{(x,y)}(\mathbf{K}, t, t') E^{(x)}(t') G(\mathbf{K}, t, t') + \text{c.c.}, \quad (\text{S38})$$

where $D^{(x,y)}(\mathbf{K}, t, t') = |d_{cv}^{(y)*}(\mathbf{K} + \mathbf{A}(t)) d_{cv}^{(x)}(\mathbf{K} + \mathbf{A}(t'))|$ and the integral becomes oscillatory by the phase kernel $G(\mathbf{K}, t, t') = e^{-i[S(\mathbf{K}, t, t') - (t-t')/T_2 + i(\phi_{cv}^{(x)}(\mathbf{K}, t) - \phi_{cv}^{(y)}(\mathbf{K}, t))]}$. By taking the time derivative via the Leibnitz's rule, we can separate the contributions proportional to the topological invariant, i.e. the Chern number:

$$J_{\text{er}}^{(y)}(t) = -i \int_{\overline{\text{BZ}}} d^2 \mathbf{K} \left\{ E^{(x)}(t) d_{cv}^{(x)}(\mathbf{K} + \mathbf{A}(t)) d_{cv}^{(y)*}(\mathbf{K} + \mathbf{A}(t)) + \int_{t_0}^t dt' \left(\partial_t D^{(x,y)}(\mathbf{K}, t, t') \right) E^{(x)}(t') G(\mathbf{K}, t, t') \right. \\ \left. + \int_{t_0}^t dt' D^{(x,y)}(\mathbf{K}, t, t') E^{(x)}(t') \partial_t G(\mathbf{K}, t, t') \right\} + \text{c.c.} \quad (\text{S39})$$

Here we used the fact that $D^{(x,y)}(\mathbf{k})e^{i(\phi_{cv}^{(x)}(\mathbf{k})-\phi_{cv}^{(y)}(\mathbf{k}))} = d_{cv}^{(x)}(\mathbf{k})d_{cv}^{*(y)}(\mathbf{k})$ and with the help of Eq. (S29), we find

$$J_{er,1}^{(y)}(t) = E^{(x)}(t) \int_{\overline{BZ}} d^2\mathbf{K} \hat{\mathbf{z}} \cdot \mathbf{\Omega}_v(\mathbf{K} + \mathbf{A}(t)). \quad (\text{S40})$$

Thus, the first harmonic has a contribution which is directly proportional to the Chern number. The second term does not show an explicit contribution to the Chern number, though that does not mean necessarily speaking that it is not related to topology. The third term leads to topological features for the harmonic emission around each cycle, i.e. in the limit that $\mathbf{A}(t') \rightarrow \mathbf{A}(t)$, noting that $D^{(x,y)}$ is the Berry curvature. This implies immediately that those harmonics emitted around a cycle with respect to the excitation time t' , should contain structural information about the Berry curvature; since this term includes a momentum integral over the whole BZ, it should also extend to the topological invariant.

S3.6 · Intra-band current and topology

By solving for the time-dependent populations n_m of Eq. (S21) and via (1), we find that the intra-band current is

$$J_{ra}^{(i)}(t) = \sum_m \int_{\overline{BZ}} d^2\mathbf{K} v_m^{(i)}(\mathbf{K} + \mathbf{A}(t)) n_m(\mathbf{K}, t), \quad (\text{S41})$$

with the m^{th} occupation, $n_m(\mathbf{K}, t)$, given by

$$\begin{aligned} n_m(\mathbf{K}, t) = & (-1)^m \sum_{j,k} \int_{t_0}^{t'} dt' E^{(k)}(t') \left| d_{cv}^{(k)}(\mathbf{K} + \mathbf{A}(t')) \right| \int_{t_0}^t dt'' E^{(j)}(t'') \left| d_{cv}^{(j)}(\mathbf{K} + \mathbf{A}(t'')) \right| \\ & \times e^{-iS(\mathbf{K}, t', t'') - \frac{t'-t''}{T_2} + i(\phi_{cv}^{(j)}(t') - \phi_{cv}^{(k)}(t'))} + \text{c.c.}, \end{aligned} \quad (\text{S42})$$

where the indices i, j, k stand for the x and y components, and $S(\mathbf{K}, t', t'')$ is the semiclassical action defined by formula (S25). The electron (hole) is excited at time t'' via the laser's electric field and the dipole matrix element. At time t' the electron and hole are de-excited, again via the driving laser field as well as the dipole. Within this time period, from t' to t , the electron and hole are accelerated in the conduction and valence bands by the driving laser field through the semi-classical velocity $v_m(\mathbf{k})$. This process leads to the harmonic emission at time t . As one can demonstrate, similarly to the inter-band current Eq. (S24), the intra-band contribution (S41) is also Bloch wavefunction gauge invariant.

Finally, our HHG spectrum is computed via the absolute square of the time-dependent Fourier transform (FT), of the inter-band $\mathbf{J}_{er}(t)$ and intra-band $\mathbf{J}_{ra}(t)$ currents.

S3.6.1 · Intra-band topology

In the limit of a 2D material, such as a Chern insulator, the intra-band current of Eq. (1) along the perpendicular emission depends explicitly on the anomalous velocity:

$$J_{ra}^{(y)}(t) = \sum_m \int_{\overline{BZ}} d^2\mathbf{K} \left[v_{gr,m}^{(y)}(\mathbf{K}, t) - E^{(x)}(t) \Omega_m^{(z)}(\mathbf{K}, t) \right] n_m(\mathbf{K}, t). \quad (\text{S43})$$

Considering the limit of a two-band model, with $n_v + n_c = 1$ for every \mathbf{K} , and in the particular case of a 2D material described by the HM, where the Berry curvature of the conduction band is the negative of the valence-band curvature, $\Omega_c = -\Omega_v$, and taking into account the anomalous velocity component, one can prove that the intra-band current associated to the Berry curvature reads

$$J_{ra,\text{Curva}}^{(y)}(t) = E^{(x)}(t) \int_{\overline{BZ}} d^2\mathbf{K} \Omega_c^{(z)}(\mathbf{K}, t) [1 - 2n_c(\mathbf{K}, t)]. \quad (\text{S44})$$

The first term is the integral of the Berry curvature over the BZ, i.e. the Chern number. The second leads as well to nonlinear effects directly associated or proportional to the topological invariant too. This term is given by $2E^{(x)}(t) \int_{\overline{BZ}} d^2\mathbf{K} \Omega_c^{(z)}(\mathbf{K}, t) n_c(\mathbf{K}, t)$, also includes the nonlinear responses, since n_c scales quadratically with the time integral of the laser field at first order of approximation, according to Eq. (S21)-(S22).

S4 · Controlling dipole discontinuities in topological phases

It is desirable the phase in front of the eigenstates in Eq. (S5), together with the Berry connections and the dipole matrix elements that derive from it, to be continuous over the entire Brillouin zone (BZ). However, this is not always possible [34]. Indeed, this is one of the core distinctions between the topologically trivial and nontrivial phases: in the nontrivial phase, it is *impossible* to find a gauge that will work smoothly for all momenta in the BZ.

In the trivial phase, in contrast, globally-smooth gauges are possible – but they are not guaranteed [62], either, so that one must always be prepared to handle discontinuities and singularities in these quantities. Moreover, as the SBEs directly

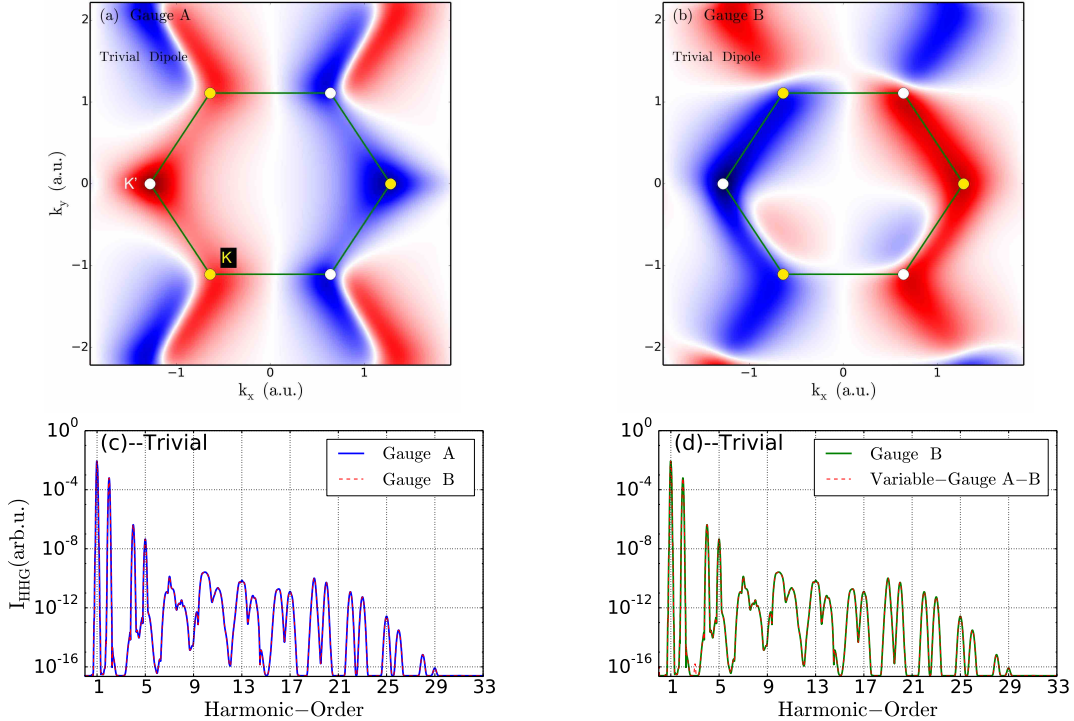


Figure S1 | Dipole matrix elements over the Brillouin zone in different gauges for a topologically-trivial phase, and the resulting harmonic spectra under a circularly-polarized laser driver. (a,b) show the real part of the x component of the dipole matrix element for two different Bloch gauges, A and B, resp. The color map ranges from dark blue to red, with white at zero. Green lines denote the hexagon of the first BZ in k space, and the K' and K points are denoted by white and yellow filled circles, resp. These two different dipoles are obviously continuous over the whole BZ for the two gauges. (c) Shows the comparison of HHG calculations using both gauge A (blue line) and B (red dashed line). (d) Same as in (c), but now the HHG calculations are performed with the variable-gauge method between gauges A and B (red dashed line) described in the text. Dipoles are calculated for HM parameters $t_1 = 0.075$ a.u., $t_2 = t_1/3$, $M_0 = 0.0635$ a.u. = $2.54t_2$ and magnetic flux $\phi_0 = 0.06$ rad, with lattice constant $a_0 = 1$ Å, giving a trivial phase with Chern number $C = 0$ and bandgap $E_g = 3.0$ eV. For the HHG spectra we drive the topological trivial phase with a left-handed circularly-polarized laser, with field strength $E_0 = 0.0045$ a.u., mean photon energy $\omega_0 = 0.014$ a.u. = 0.38 eV (corresponding to $\lambda = 3.2$ μm), with a gaussian envelope lasting $N_c = 14$ cycles at FWHM and carrier-envelope phase fixed to zero, with the specific form given in Eq. (S23). We use a dephasing time of $T_2 = 220$ a.u. Our momentum grid, for integration, uses $N_x = 873$ by $N_y = 511$ points, with boundaries at $k_{x,\max} = \frac{2\pi}{\sqrt{3}a_0}$ and $k_{y,\max} = \frac{2\pi}{3a_0}$; for the SBE time integration our timestep is $dt = 0.1$ a.u. We use a two-dimensional Simpson rule to integrate the final currents over the BZ.

incorporate these two quantities (see Eqs. (S21) and (S22)), the numerical calculations of the currents can inherit that artificial singularities, leading to unstable harmonic plateau or cut-off. Here we show an example of how this numerical instability arises, and the method we use to solve it. This method relies on the control of the localization of the dipole discontinuity in the BZ by choosing different gauges for different subsets (in the language of differential geometry, for different charts [63]) of the BZ.

Figures S1(a) and S1(b) show the real part of the x component of the dipole matrix element, $d_{cv}^{(x)}(\mathbf{k})$, of a trivial topological phase, taken in two different gauges: A, where $\mathbf{B}'_{\mathbf{k},A} = (B_{2,\mathbf{k}}, B_{3,\mathbf{k}}, B_{1,\mathbf{k}})$, and B, where $\mathbf{B}'_{\mathbf{k},B} = (B_{3,\mathbf{k}}, B_{1,\mathbf{k}}, B_{2,\mathbf{k}})$. As can be seen there, both gauges exhibit substantially different dipoles, but their corresponding harmonic emissions – shown in Fig. S1(c) – are absolutely the same, i.e. the emission is gauge invariant, as expected. This is a simple and obvious test, but a powerful mathematical property which will help us to avoid misleading interpretations of the HHG numerical outcomes from topological phases, where singularities are unavoidable. Figure S2 shows similar results for a topologically-nontrivial phase. Most prominently, in the dipole maps of Fig. S2(a) and S2(b), we notice pronounced discontinuities in the dipole, which are highlighted by the turquoise circles and shown in detail in the inset plots, and which appear in both gauges. Secondly, the HHG calculations for gauges A and B, shown in Fig. S2(c), show numerical noise around the plateau at HO > 5th and, more troublingly, a lack of a well-defined cut-off. These features signal a numerical instability of the calculation, which is independent of the numerical convergence of our 5th-order Runge–Kutta method.

To solve this problem, we use the fact that the k -space discontinuities in the dipole can be shifted within the BZ (as shown in Fig. S2(a) and S2(b)) by choosing different gauges: the existence of singularities is inevitable (or wavefunction phase zeros [34]), but their location is not physical and it can be moved by switching phase conventions, so we use different gauges to calculate the SBE evolution in different patches of the BZ, and then coherently combine the currents at the end of the calculation. Thus, in our variable-gauge technique, we use the two gauges described above, A and B, for the different BZ regions where each gauge is regular, using the following three steps:

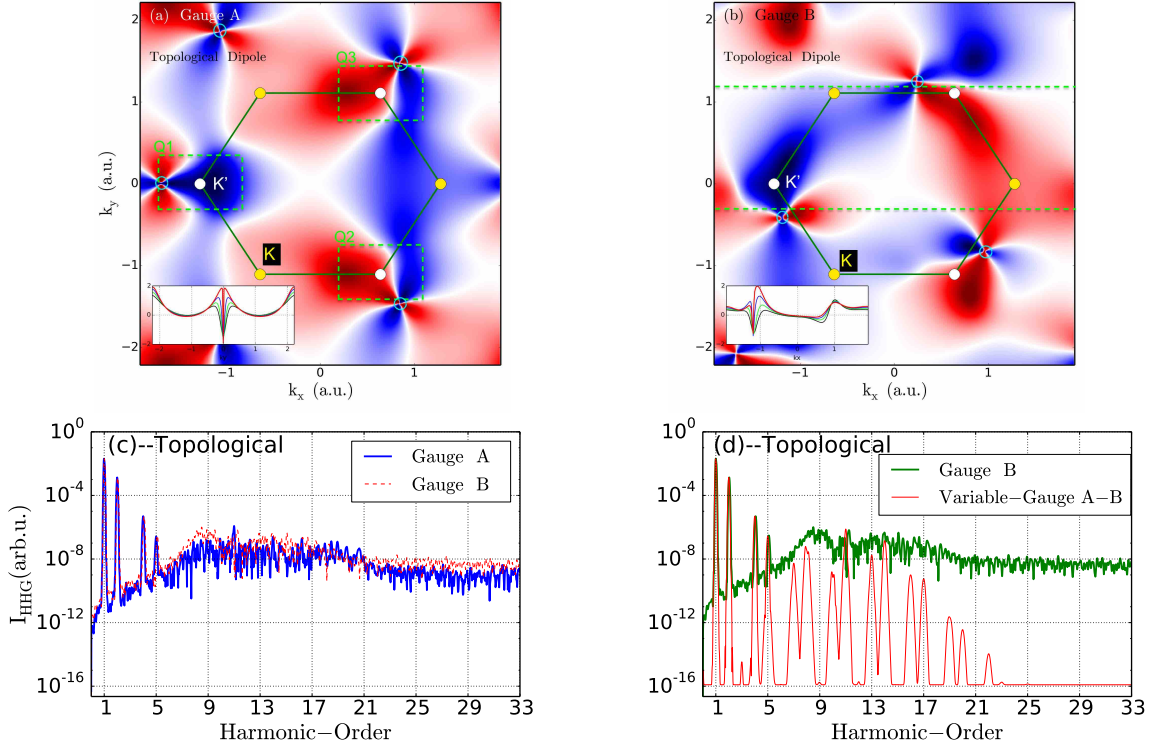


Figure S2 | Dipole matrix elements and the resulting harmonic spectra, similarly to Fig. S1, for a topologically-nontrivial phase with $C = +1$. In (a) we include insets showing cuts through the singularities of the dipole, along k_y at fixed $k_x = -1.85$ (black), -1.80 (green), -1.75 (blue) and -1.70 a.u. (red), and similarly for (b), with vertical cuts at fixed $k_y = -0.55$ (black), -0.50 (green), -0.45 (blue) and -0.40 a.u. (red). Both gauge A and gauge B exhibit discontinuities within the BZ we use to compute the harmonic response; turquoise circles indicate their locations. The green boxes Q1, Q2 and Q3 around the K' points denote the BZ regions in which HHG calculations might pick the discontinuity up or not. In (c) and (d) we show the harmonic spectrum produced by a left-circular driving laser, with the same parameters as in Fig. S1. In (c) we compare the HHG using gauges A (blue line) and B (red dashed line) independently, while (d) depicts HHG for gauge B (green line) and for our variable-gauge technique (red line). The parameters are the same as in used in Fig. S1, with the exception of $\phi_0 = 1.16$ rad.

- Gauge A for the BZ region which falls into $-k_{y,\text{max}} \leq k_y \leq \epsilon_{y,1}$, where $\epsilon_{y,1} = -0.35$ a.u. is marked with the horizontal green dashed line in Fig. S2(b).
- Since all physical quantities are periodic within the whole BZ, the regions Q1, Q2 and Q3 (as marked in Fig. S2(a)) are physically equivalents, we use gauge A shifted to the Q3 region when k_y satisfies $\epsilon_{y,1} < k_y \leq \epsilon_{y,2}$, where $\epsilon_{y,2} = 0.02$ a.u.
- Gauge B for momenta which satisfy $\epsilon_{y,2} < k_y \leq k_{y,\text{max}}$.

We compute HHG with this variable-gauge method for both the trivial and topological phases. For the trivial phase, we show the resulting harmonic spectrum in Fig. S1(d), where the red dashed line shows the variable-gauge results; we find very good agreement between this approach and the fixed-gauge reference (using gauge B), which works well for the trivial phase, as discussed above, and thus serves as a benchmark for the variable-gauge approach.

With this in place, we can confidently apply the same technique to the calculations of the HHG for the topological phase, the results of which are shown in the red line of Fig. S2(d). The HHG spectrum for this topological phase shows a clean plateau with well-defined harmonics and a clear cut-off region, and, moreover, a clear numerical threshold, in comparison to the fixed-gauge method using gauge B. Our numerical threshold is fixed at $I_{\text{HHG}} \approx 10^{-16}$ arb. u., but we have found that this threshold can be reduced up to 10^{-25} arb. u. for the HHG yield, depending on the parameters used for the BZ grid and the time integration.

That said, it is important to note that, while our variable-gauge method can map very well the plateau and cut-off for topological phases, at the critical point of the Haldane model – where the bandgap closes, at the topological phase transition – our method finds an undefined harmonic cutoff, as shown in Fig. 4 of the main text. This is also expected, since the closing of the bandgap creates an undetermined dipole matrix element at the Dirac cone, where the population is most easily transferred to the conduction band.

S5 · Linear field scaling of the high harmonic cut-off

In order to validate our theoretical model and numerical variable-gauge methods, we investigate how the HHG emission cut-offs for the total, intra-band and inter-band contributions behave as a function of the laser field strengths, for both trivial and topological phases.

Figures S3(a,b) show the results for the total harmonic emission $I_{\text{HHG}}(\omega) = \omega^2 [|J^{(x)}(\omega)|^2 + |J^{(y)}(\omega)|^2]$ of the trivial and nontrivial topological phases. First, we see a clear linear cut-off in terms of the laser strength for the topological trivial case. This tendency is in very good agreement with the pioneering experimental observation of Ref. 17 and the theoretical confirmation by Vampa et al. in Refs. 21, 58. In the case of the topological phase, we observe a linear cut-off scaling as a function of the laser field strength, similar to the trivial one.

We also depict, in Figs. S3(c,d), the corresponding intra-band harmonic emissions for trivial and non trivial phases, via the group and anomalous velocity emissions. We find the intra-band for the topological emission seems to exhibit a much larger intensity yield than the trivial phase (though the coupling between the two also needs to be considered in more detail [23]). This is expected since the topology will show up clearly in the intra-band currents via the anomalous velocity, as demonstrated by the analytical considerations from Eqs. (S41-S44).

In contrast, Figs. S3(e,f) show that, for our excitation conditions, the inter-band contributions for the trivial and topological phases dominate around the plateau and cut-off in comparison to intra-band emissions. One therefore needs to carefully consider and analyze the inter-band mechanism for high nonlinear emission, i.e. HO > 5th, and not uniquely the intra-band mechanism. Figs. S4(a,b) show the relative asymmetry between the inter-band and intra-band currents for trivial and topological phases. The latter show clearly that the inter-band mechanism is largely dominant for the plateau and the cut-off of the HHG spectrum. This is an important observation since, for instance, retrieving the Berry curvature from a measurement scheme, will require the ability to distinguish between intra-band and inter-band emission mechanisms.

S6 · Harmonic emission in α -quartz

In order to extract a better physical insight behind our theoretical validation via α -quartz, we will show different calculations of inter- and intra-band currents. As explained in the above section, the HM allows us to break both IS and TRS [33]. Once IS is broken and TRS is protected, the topological invariant is zero, $C = 0$, but the Berry curvature is not.

For IS breaking, we choose a simplest set of HM parameters to reproduce the band-gap $E_g \sim 9$ eV of SiO₂ [26]. Fig. 2 of the main text shows this experimental and theoretical comparison. We have described two observations about this comparison in

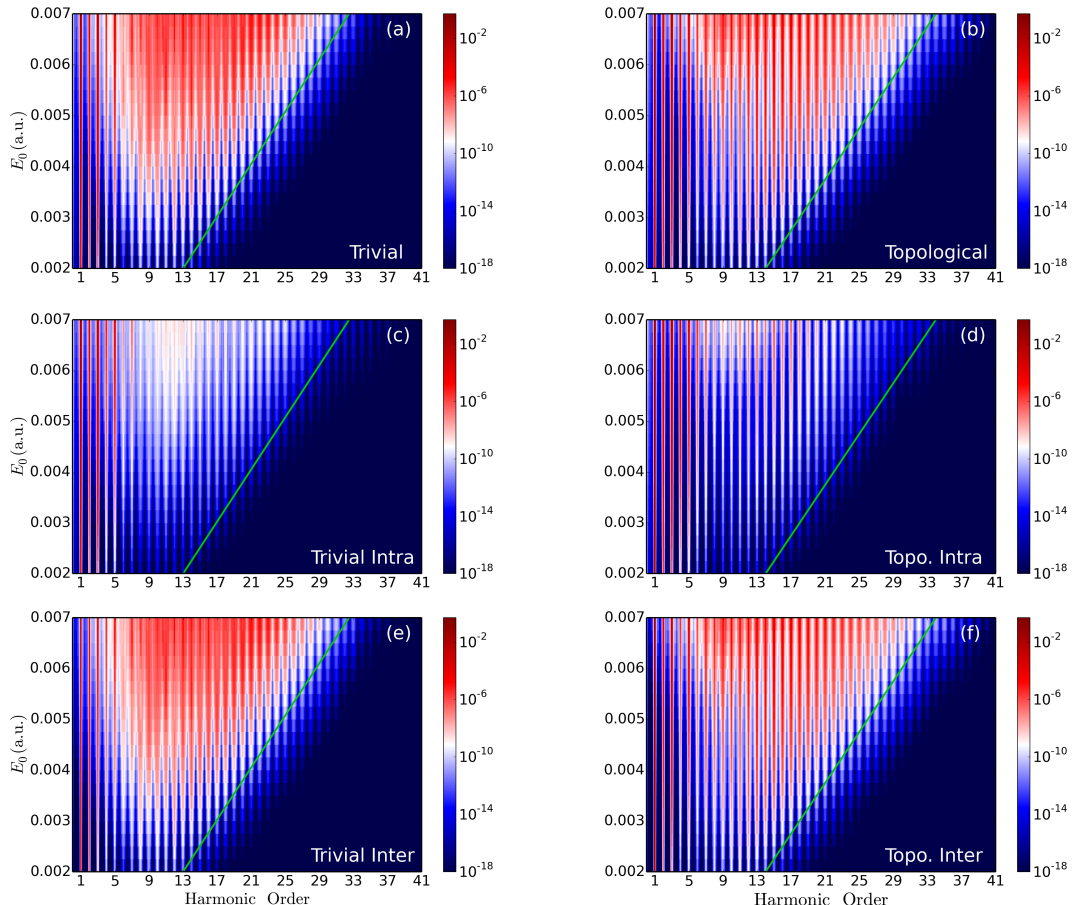


Figure S3 | Trivial and topological high harmonic cut-off law for linear polarized driving fields. Total HHG emissions for trivial and topological phases, with same HM parameters than the used in Fig. (S1) and Fig. (S2), as a function of the laser field strength E_0 are depicted in (a) and (b), respectively. (c) And (e) show the decomposition of the total harmonic emission for the intra-band and inter-band currents emissions of the trivial phase, respectively. (d) And (f) depict the intra-band and inter-band current emissions for the topological phase. Green lines mimic the linear-cut off for both trivial and topological phases. Our laser field for these HHG calculations is linearly polarized along $K' - \Gamma - K$ direction of the honeycomb hexagonal lattice.

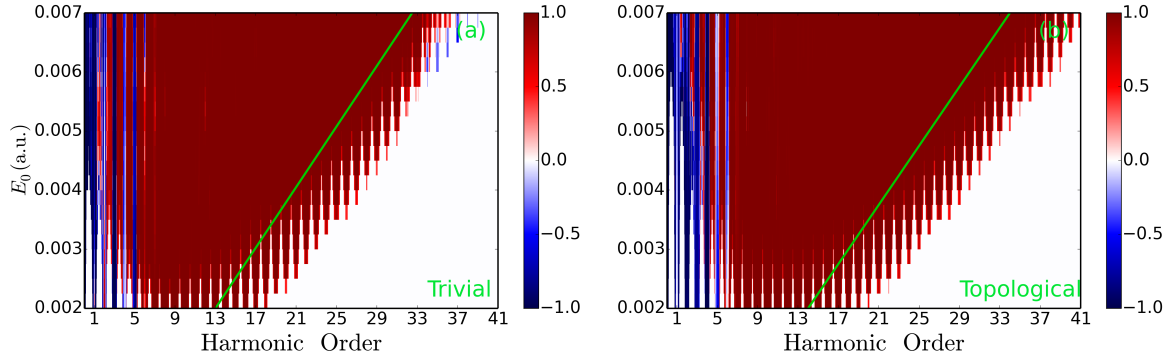


Figure S4 | Inter-to-intra-band asymmetry emission for trivial (a) and topological (b) phases driven by a linearly-polarized laser pulse. Asymmetry of the inter-band and intra-band emission defined by $I_{\text{er-ra}} = \frac{I_{\text{er}}(\omega) - I_{\text{ra}}(\omega)}{I_{\text{er}}(\omega) + I_{\text{ra}}(\omega)}$ calculated for the parameters and spectra shown in Fig. (S3).

the main text: first, even and odd harmonics appear in the polarization integration measurement; and, secondly, even harmonics show smaller harmonic yields. Hence, we find a relatively good qualitative agreement for low-order harmonics between our model and the experiment by Luu & Wörner. That said, it is important to note that the calculations overestimate the intensity yield for the high-order harmonics (HOs) of the plateau.

That discrepancy between theory and experiment is related to the limitation of this toy model under the tight-binding approach, which will not recreate the whole experimental complexity for the following reasons: (i) the lattice crystal is not a monolayer (the crystal thickness is 20 μm [26]), (ii) the crystalline structure of the hexagonal 3D lattice of SiO_2 is much more complex than our simplified 2D lattice, (iii) the possibility of higher conduction bands and lower valence bands playing a role is not considered in our approximations [64], (iv) the propagation effects in the 20 μm -thick crystal can play a fundamental role [65], and (v) finally, this is a simple proof-of-concept test, and not the ultimate potentiality of the HHG approach presented in the this paper. However, despite this discrepancy, we believe that physical insight can be extracted in terms of identifying dominant mechanisms for the harmonic emission – (intra-band) nonlinear Bloch oscillations of charge carriers [23], and (inter-band) electron-hole recombination processes [18], and their relative importance.

We now turn to the parallel and perpendicular components of the harmonic emission when driven by a linearly-polarized laser, with respect to the driver's polarization, which we show in Fig. S5 broken out into the intra- and inter-band components. Firstly, our calculations show the same qualitative features of the experiments [25, 26]: odd and even harmonics are emitted along the parallel and perpendicular emission directions, respectively. Secondly, the inter-band current dominates over the intra-band one for both parallel and perpendicular configurations, at least for these excitation conditions, and with the usual caveats regarding the nontrivial coupling between the two components [23]. This implies that a recollision mechanism is likely to be at play in a system where the IS is broken. We also note that along the perpendicular emission HHG shows only even harmonics for the intra-band analysis exhibiting dominant behavior for largest harmonic orders (HOs). We believe that the appearance of even harmonics along the perpendicular direction is not only a matter of intra-band or Berry curvature effect: it is produced by the inter-band process: a combination of dipole phases, Berry curvature and Berry connection features, as our

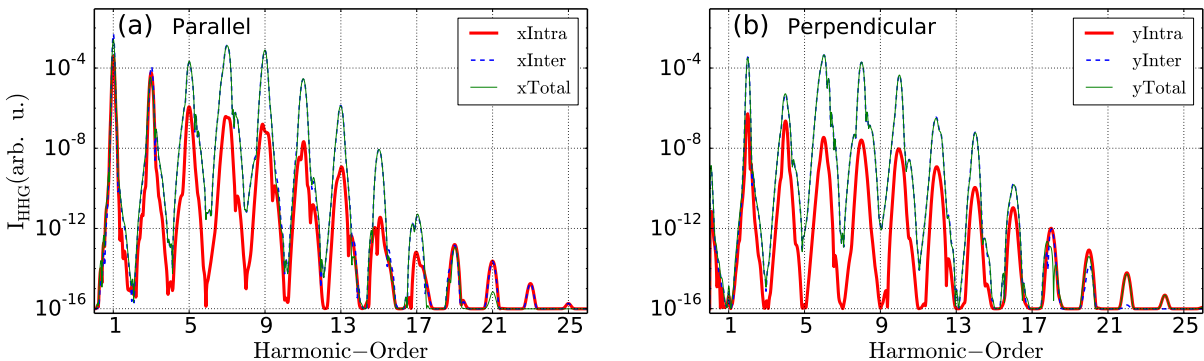


Figure S5 | Parallel (a) and perpendicular (b) harmonic emission from our α -quartz toy model. Inter-band, intra-band and total (inter + intra) harmonic spectra are depicted in blue, red and green lines, respectively. The laser-field parameters used are similar to those in the experiment, i.e. laser wavelength $\lambda_0 = 800 \text{ nm}$ giving a central frequency $\omega_0 = 0.056 \text{ a.u.} = 1.53 \text{ eV}$, FWHM duration of 10 cycles under a Gaussian envelope, and peak intensity of $I_0 = 3.2 \times 10^{12} \text{ W/cm}^2$. Our driving laser is linearly polarized along the $\text{K}' - \Gamma - \text{K}$ direction of the hexagonal crystalline direction in the BZ. In these calculations a dephasing time of $T_2 = 220 \text{ a.u.}$ (5.3 fs) was used. We use a honeycomb lattice with lattice constant $a_0 \sim 4.8 \text{ \AA}$, NN hopping $t_1 = 2.1 \text{ eV}$, NNN hopping amplitude $t_2 = 0.36 \text{ eV}$ with magnetic flux $\phi_0 = 0$, and staggering potential $M = 4.5 \text{ eV}$, with a band gap $E_g \sim 9 \text{ eV}$.

saddle-point arguments for the inter-band mechanism and the numerical calculations here have suggested. The HHG emission is not only the product of a single effective intra-band contribution – both inter-band and intra-band mechanisms are present in the rich physics of this non-linear harmonic emission process.

S7 · Dephasing time in the harmonic emission for topological phases

We now study the role of the dephasing time T_2 on the circular dichroism (CD, see Eq. 3 in the main text) for the trivial and topological phases. Figures S6(a,b) show the HHG spectra as a function of T_2 for trivial and nontrivial topological phases, respectively. The emitted harmonic intensity is sensitive to the dephasing time, as shown also in literature for linearly polarized lasers [58]. Here we also observe sensitivity of the HHG emission yields with respect to T_2 for both trivial and topological phases. T_2 usually reduces the coherence of the occupations and therefore also the electron-hole recombination mechanisms, more strongly for long trajectories [58].

We believe the same effects take place in topological phases under this simple two-band approximation, which would lead to a potential dependence of the dichroism for the different harmonic orders. Additionally, we computed also HHG for the case $T_2 \rightarrow \infty$ (not shown, for simplicity), in which case the harmonic plateau becomes extremely noisy. The later makes impossible to extract any reliable physical quantity from the simulations. This can be also noticed in the numerical background noise of Fig. S6(b) as the dephasing time increases.

Trivial Circular Dichroism:

For the trivial phase, Figs. S6(c,e) show the dichroism as a function of T_2 for $3n+1$ (co-rotating HO) and $3n+2$ (contra-rotating HO) HOs, respectively; we find a strong dependence of the CD on the dephasing time for each individual order. Nevertheless, when averaging the CD for co-rotating orders over T_2 , it remains negative, providing a systematic tendency around the plateau and, likely, the cut-off. In contrast, for the contra-rotating orders, CD oscillates between positive and negative values depending on lowest or highest region of the spectrum. We believe this behaviour is a natural consequence of the complex relationship

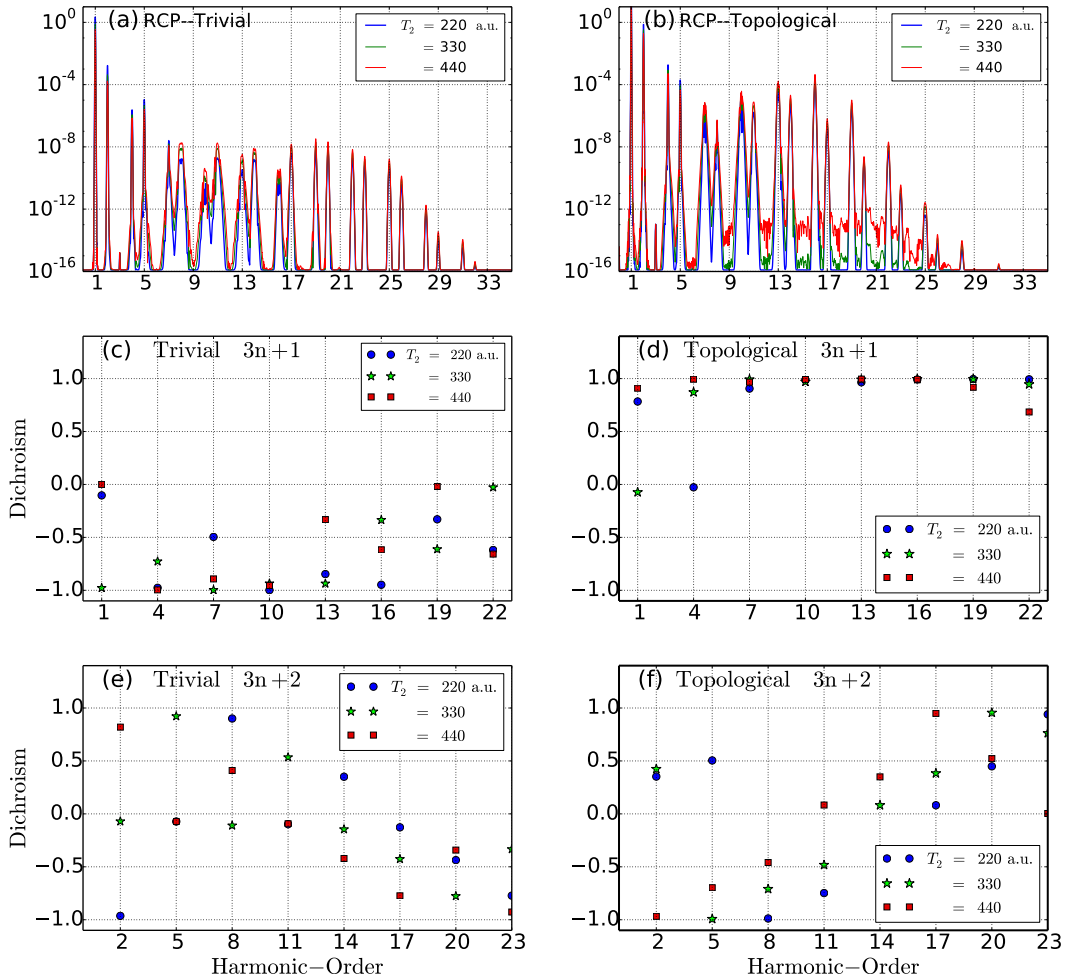


Figure S6 | Role of the dephasing time in the high-harmonic emission and in its circular dichroism. (a,b) HHG spectra for various dephasing times T_2 , for trivial and topological phases, respectively, driven by a right-circularly polarized laser. (c-f) Circular dichroisms for $3n+1$ (co-rotating) and $3n+2$ (contra-rotating) harmonic orders ((c,d) and (e,f), resp.), for trivial (c,e) and topological (d,f) phases. The parameters for the material and the driving laser are the same as in Fig. S1 with a slightly altered peak field strength, $E_0 = 0.005$ a.u., and pulse duration, $N_c = 16$.

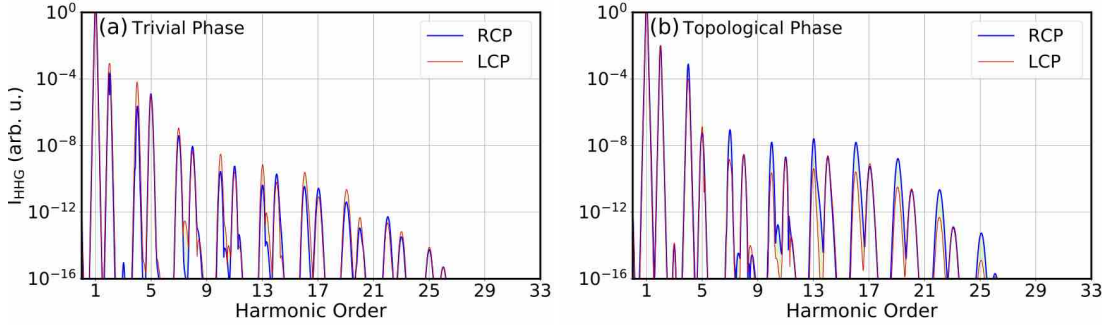


Figure S7 | High harmonic generation and circular dichroism in the electromagnetic minimum-coupling gauge. (a,b) Harmonic emission produced by left- and right- circularly polarized (LCP and RCP) lasers for trivial and topological phases, respectively – see Fig. (3a) and (3b) of the main text and consider that the matter and laser parameters are used here.

between the electron-hole recombination mechanism, intra-band and inter-band mechanisms and the T_2 .

Topological Circular Dichroism:

In contrast, the co-rotating CD shown in Fig. S6(d) is much more robust against T_2 for the topological phase; exhibiting values around +1, most noticeably when HO > 4th. For contra-rotating orders (see Fig. S6(f)), the CD describes ‘similar features’ across the whole spectrum as in the trivial phase. In that sense the CD depends on the harmonic region, low, plateau or cut-off regions. These observations show that the CD is a more robust quantity for the co-rotating than for the contra-rotating harmonic orders; this is our main reason for focusing on the CD of the former in the main text.

S7.1 · Circular dichroism in the minimum-coupling gauge

In order to stress that the circular dichroism (CD) of the high nonlinear optical responses is an excellent quantity to distinguish topological phases of matter, in this section we show its electromagnetic laser-field gauge invariant features. To this end, we calculate the HHG using the minimum-coupling gauge or velocity gauge (VG) formalism described in Ref. [62] under the laser-matter Hamiltonian $H(t) = H_0 + \mathbf{p} \cdot \mathbf{A}(t) + \mathbf{A}^2(t)/2$, where \mathbf{p} is the quantum mechanic momentum operator. This VG (more precisely VG in the SBEs) picture is adapted to the topological Haldane model for the same conditions of Fig. (3a) and (3b) described in the main text (the electromagnetic length gauge (LG or more precisely LG in the SBEs) is used across the main text).

The results for trivial and topological phases are shown in Fig. (S7a) and (S7b). We find qualitatively good agreement between the harmonic responses produced by VG and LG (see Fig. 3 of the main text), as expected. This is simply understood in terms of two facts: (1) since the approximated Haldane Hamiltonian H_0 is by construction truncated to two bands, the Thomas-Reiche-Kuhn sum rule [66] is obviously broken – to guarantee fully quantitative agreement, either corrections or a large number of bands are required [66, 67], which by definition is impossible for Haldane model. Thus, these two-band VG and LG models are expected to agree at the qualitative level that is in perfect analogy to the gas phase, as shown by Pérez-Hernández *et al.* for S-Matrix approach of HHG [68]. (2) The dephasing time might play a different role in VG.

Note, however, we find that VG *circular dichroisms* for co-rotating harmonic orders are in very good agreement with those produced by the LG (see Fig. (3a) and (3b) of the main text), beside other characteristics such as the asymmetric pattern of the relative intensity weight between the co-rotating and contra-rotating orders; particularly, across the plateau of the spectrum, i.e. HOs 10th–22th. From Fig. (S7) clearly, the CD is negative for the trivial phase, while positive (CD \approx +1) for the topological phase across the 3n + 1 HOs of the plateau.

To summarize, the latter observations about the *circular dichroisms* of the co-rotating orders are impressive evidences to support that this quantity is fully invariant under the electromagnetic gauge, hence, free of any mathematical or un-physical artifact for the conclusions presented in our paper. This adds then an extra argument to propose the CD of HHG to distinguish topological phases of matters and transitions.

S8 · Quasi-classical trajectory analysis

Here, we apply saddle-point approximation (SPA) to extract better physical insight of the electron-hole emission within the two different topological phases of the HM, i.e. trivial and non-trivial topological materials. The energy of the emitted photon, Eq. (S37), and the displacement between the electron and hole trajectory, Eq. (S32), are reproduced here, as

$$\omega(\mathbf{k}(t), t) = \varepsilon_g(\mathbf{k}(t)) + \omega_c(\mathbf{k}(t), t), \quad (\text{S45})$$

$$\Delta\mathbf{x}_c(\mathbf{k}, t, t') - \Delta\mathbf{x}_v(\mathbf{k}, t, t') = \int_{t'}^t \tilde{\mathbf{v}}(\mathbf{k}(t''), t'') dt''. \quad (\text{S46})$$

Here $\tilde{\mathbf{v}} = \tilde{\mathbf{v}}_g + \tilde{\mathbf{v}}_c + \tilde{\mathbf{v}}_a$ is electron-hole velocity difference of the SPA inter-band current, $\tilde{\mathbf{v}}_g = \mathbf{v}_{gr,c} - \mathbf{v}_{gr,v}$ the group velocity, which separates naturally into connection $\tilde{\mathbf{v}}_c = (\mathbf{E} \cdot \nabla_{\mathbf{k}}) \left(\xi_g + \nabla_{\mathbf{k}} \phi_{cv}^{(j)} \right)$ and anomalous $\tilde{\mathbf{v}}_a = \mathbf{v}_{a,c} - \mathbf{v}_{a,v}$ components (where

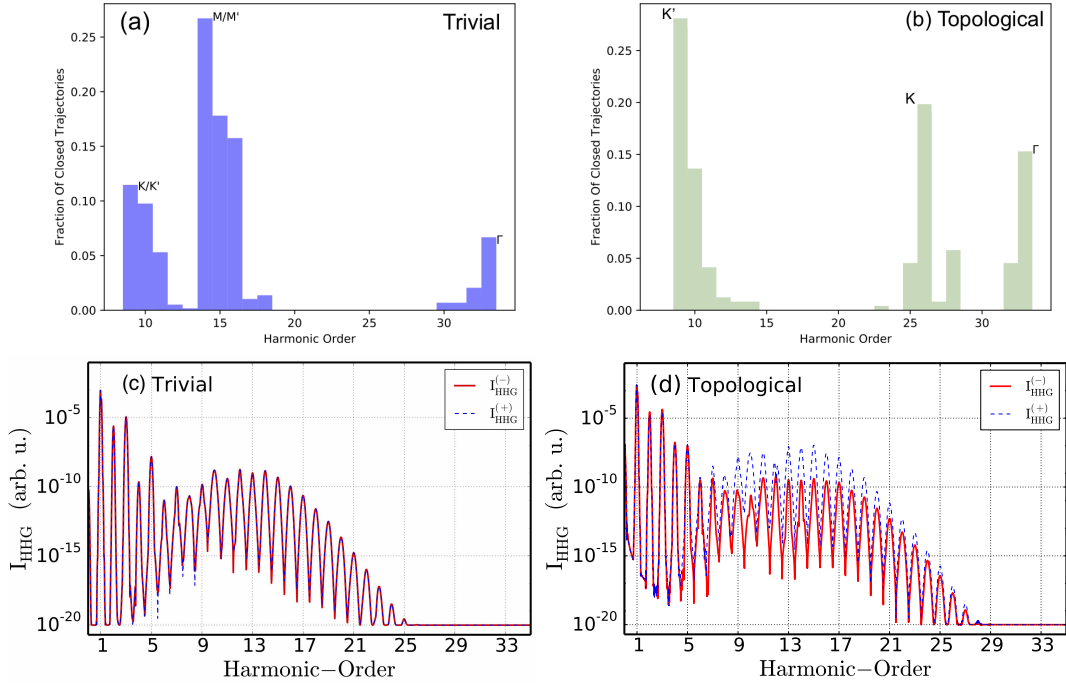


Figure S8 | Quasi-classical analysis of the harmonic emission for different topological phases driven by a linearly-polarized field. The fraction of closed trajectories Eq. (S32) at a given recombination energies or harmonic order emission are shown in (a) and (b) for the trivial and topological phases, with equal band gap of $E_g = 3.45$ eV. These calculations are conducted by numerically integrating Eq. (S46) and determining if $|\Delta x(t)| < \epsilon$. A closed electron-hole trajectory is found once the condition $\epsilon \sim 10^{-3} a_0$ is fulfilled. In (c) and (d) we show the corresponding HHG spectra for the two topological phases of (a) and (b), driven by a linearly-polarized laser field of strength $E_0 = 0.003$ a.u. and frequency $\omega_0 = 0.014$ a.u., lasting $N_c = 14$ optical cycles at FWHM under a Gaussian envelope.; we use a dephasing time of $T_2 = 220$ a.u. We decompose the harmonic emission into its circular components $I_{\text{HHG}}^{(\pm)}(\omega) = \omega^2 |J^{(x)}(\omega) \pm i J^{(y)}(\omega)|^2$, with the positive (negative) sign indicating right-handed (left-handed) circular component, depicted by the blue dashed (red solid) line. The emission's helicity for the trivial phase, $C = 0$ and $\phi_0 = 0$, is zero along the whole harmonic spectrum, while for the topological phase, $C = +1$ and $\phi_0 = \frac{\pi}{2}$, the emission's helicity changes from positive to negative across the spectrum.

$v_{a,m}(\mathbf{k}) = -\mathbf{E}(t) \times \Omega_m(\mathbf{k})$ is the anomalous velocity); there is also a contribution to the energy, $\omega_c = \mathbf{E} \cdot (\xi_g + \nabla_{\mathbf{k}} \phi_{cv}^{(j)})$, which one can identify as a “connection energy” (which also includes a contribution from the phase of the dipole moment, $\phi_{cv}^{(j)}$, to keep it gauge-invariant). Both the emitted photon energy ω and the electron-hole trajectory evolution $\Delta x_m(t)$ depend on time through the evolution of the lattice momentum $\mathbf{k}(t)$ and the electric field $\mathbf{E}(t)$. We will first study the trivial phase, i.e. $C = 0$, where the terms ω_c , \tilde{v}_c and \tilde{v}_a have an explicit dependence on $\mathbf{E}(t'')$ which is small. For a linearly polarized electric field in the x direction, k_x is bounded by $k_{x0} \pm 2A_0$, depending on when in time and in the BZ the electron-hole pair are created or annihilated. (Here A_0 is the vector potential amplitude $A_0 = \frac{E_0}{\omega_0}$.) We first note that a recombination saddle-point condition occurs only when the momentum $\mathbf{k}(t'')$ covers a line within the BZ in which $\tilde{v}(\mathbf{k})$ changes its sign. Secondly, if A_0 is small compared to the size of the BZ, then the emission energy will be approximately determined by the excitation momentum, as $\omega \approx \omega(\mathbf{k}_0)$. To determine when $\tilde{v}(\mathbf{k})$ changes sign, we depict in Fig. S9 the zeros of $\tilde{v}_x(\mathbf{k})$ and $\tilde{v}_y(\mathbf{k})$, and identify their intersection. The intersections of x - and y -direction velocities are at the BZ points K' , K , M , M' and Γ . Hence, close to these intersections, one would expect that an electron-hole excited with \mathbf{k}_0 will recombine. This is shown in Fig. S9 and also suggests, we should expect harmonics around 10, 15 and 30th associated with the points K , M and Γ . In addition, we search all creation momenta \mathbf{k}_0 and times t' for trajectories which satisfy SPA and compute the fraction of recombination trajectories with emission energy; this is depicted in Fig. S8. Here, we confirm the above approximation, with the bulk of the emission coming from around the K , M and Γ points. This is further confirmed, in this trivial phase, by Fig. S8(a,b) and by our numerical fully quantum-mechanical calculations of HHG shown in Figs. S8(c,d). However, the classical trajectories corresponding to real \mathbf{k}_0 and times t' are thus not capable of producing the harmonic orders 20-30th for the trivial topological phase. We assume these are due to quantum mechanical effects described by complex-valued \mathbf{k}_0 and t' saddle points, similar to the complex-trajectory effects that are known to have important roles in atomic strong-field phenomena [69]. Furthermore, we note that the HHG emission for the trivial phase driven by linearly-polarized fields is linearly polarized throughout the spectrum, at least for the $\phi_0 = 0$ case shown here. The emission by the linearly-driven topological phase shown in Fig. S8(d), on the other hand, has a nonzero helicity – indicated by the dominance of one of the circular components over the other – and this varies over the spectrum, as described in more detail by Silva et al. [43].

For the nontrivial phase, \tilde{v}_c and \tilde{v}_a are not small, and therefore the intersection of the zeros of \tilde{v}_x and \tilde{v}_y will have an explicit

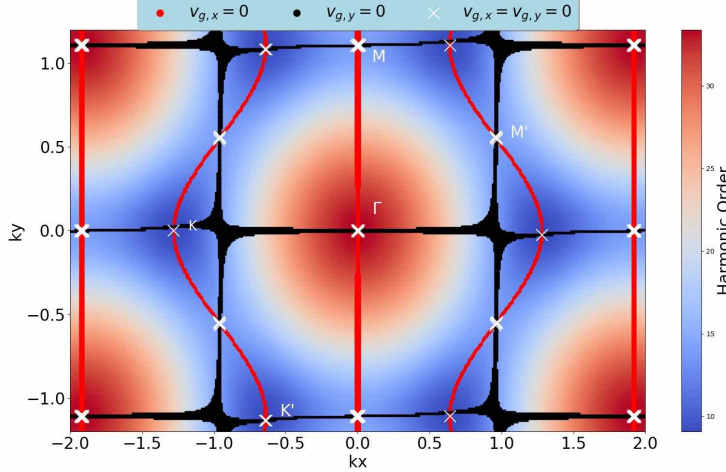


Figure S9 | Trivial topological phase, $C = 0$. Here, in color-scale, we depict the recombination energy at $M_0/t_2 = 2.54$, $\phi_0 = 0$ as a function of the crystal momentum \mathbf{k} . We have also marked the zeros of the x and y components of the total velocity $\tilde{\mathbf{v}}$ in red and black dots. White crosses denote the intersection between x and y velocity components. The points K , K' , Γ and M are marked with white crosses.

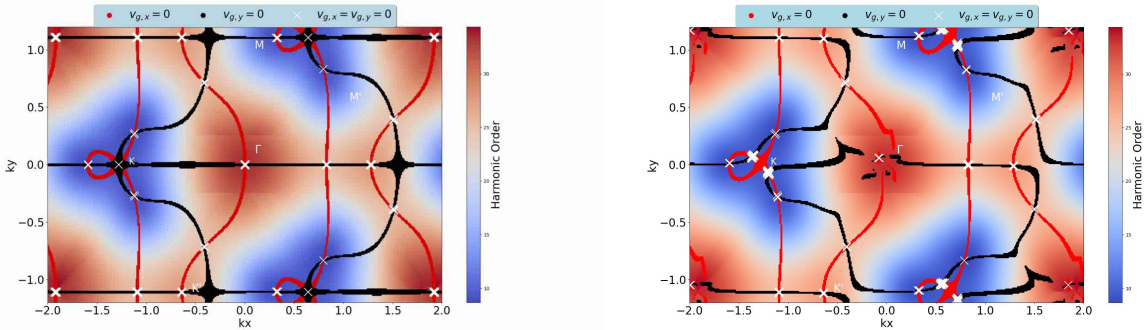


Figure S10 | Non-trivial topological phase, $C = +1$. We depict the recombination energy (harmonic order) for $M_0/t_2 = 2.54$, $\phi = \pi/2$ and $E_x(t_0) = 0$ (left) and $E_x(t_{\max}) = 0.003$ a.u.. We mark the zeros of the x and y components of $\tilde{\mathbf{v}}$ in red and black dots. For t_{\max} , the connection velocity $\tilde{\mathbf{v}}_c$ depends on the dipole phase $\phi_{cv}^{(x)}$, and dramatically modifies the intersections near the K point. The modification of the velocity near the Γ point is unphysical – it is a numerical artifact caused by the dipole magnitude going to zero (resulting in an undefined dipole phase).

dependence on t'' . To adapt the above analysis for the non-trivial topological phase, i.e. Chern number $C = +1$, we show the zeros and intersections at two excitation times: $t'' = t' = t_{\max}$ when $E_x(t_{\max}) = E_0$, and $t'' = t' = t_0$ when $E_x(t_0) = 0$. Excitations for the latter case $E_x(t_0) = 0$ are less probable. First, we note that for the excitation time t_0 , the band structure has dramatically changed (see Fig. S10) from the trivial case we examined above. The intersection at the M point has shifted closer to the K point and the intersection at the M' point has split and shifted toward both of the K points. We again have three sets of intersections around similar energy. Those bunched around the K , K' and Γ points. The most dramatic difference is that the energy around the K' point has moved up to the 20th – 30th harmonic and we thus expect to see closed trajectories with emission energies of this order, while we will no longer see them for the 15th-20th harmonics. Secondly, at the excitation time t_{\max} most intersections are unchanged from t_0 , and thus we have similar expectations for the closed trajectories. The main difference is the intersection that was on the K' point has split into two, and will thus be changing as time evolves. We can thus expect that the integrand changes sign for a greater range of \mathbf{k}_0 and that these trajectories will be more complicated.